Electronic Supplementary Material (ESI) for Energy & Environmental Science.
This journal is © The Royal Society of Chemistry 2021

Formamidine disulfide oxidant as a localised electron scavenger for >20% perovskite solar cell modules

Jun Zhu,[a†] Seulyoung Park,[b†] Oh Yeong Gong,[b] ChangHwun Sohn,[b] Zijia Li,[a] Zhenru Zhang,[a,c] Bonghyun Jo,[b] Wooyul Kim,[c] Gill Sang Han,[b] Dong Hoe Kim,[d] Tae Kyu Ahn,[*a] Jaichan Lee,[*b] Hyun Suk Jung[*b]

[a] Department of Energy Science, Sungkyunkwan University (SKKU), Suwon, 16419, Republic of Korea

[b] School of Advanced Materials Science and Engineering, Sungkyunkwan University, Suwon 16419, Republic of Korea

[c] Department of Chemical and Biological Engineering/Research Institute of Global Environment, Sookmyung Women's University, Seoul 04310, Republic of Korea

[d] Department of Nanotechnology and Advanced Materials Engineering, Sejong University, Seoul 05006, Republic of Korea

†These authors contributed equally

*Correspondence: hsjung1@skku.edu (H.S.J.), jclee@skku.edu (J.L.) taeahn@skku.edu (T.K.A.)

Materials

Fluorine-doped tin oxide (SnO_2:F, FTO) was purchased from Pilkington (TEC8, 8Ω sq^{-1}). Titanium tetrachloride ($TiCl_4$), dimethyl sulfoxide (DMSO, 99.9%), acetonitrile (99.8%), dimethylformamide (DMF, 9.8%), chlorobenzene (CB, 99%), toluene (99.8%), diethyl ether (99.7%), lithium bis(trifluoromethanesulfonyl)imide salt (Li-TFSI), acetonitrile (ACN, 99.8%), and 4-tert-butylpyridine (tBP) were purchased from Sigma-Aldrich (USA). PbI_2 (99.995%), $PbBr_2$ (99%), and formamidine disulfide dihydrochloride (FASCl, >98.0%) were purchased from TCI. $HC(NH2)_2I$ (FAI), CH_3NH_3Br (MABr), and methylammonium chloride (MACl) were purchased from Greatcell solar. The 2,2',7,7'-tetrakis (N,N-di-p-methoxyphenylamine)-9,9'-spirobifluorene (Spiro-OMeTAD, LT-S922) was purchased from the Luminescence Technology Corp. Poly[bis (4-phenyl)(2,4,6-trimethylphenyl)amine] (PTAA, Mn = 3200, Mw = 4900) and oleylammonium iodide were purchased from Xi'an Polymer Light Technology Corp (China). All materials were used as received without post-treatment or further purification.

Synthesis of perovskite powder

Perovskite powder was synthesised by modifying a procedure reported in a previous study.[1] For $FAPbI_3$ powder synthesis, 7.66 g of FAI was added to an Erlenmeyer flask containing 150 mL acetonitrile (ACN) under vigorous stirring; then PbI_2 (15.79 g; PbI_2:FAI = 1:1.3) was slowly added together with an extra 50 mL of ACN. A brown precipitate appeared after the addition of PbI_2. After vigorous stirring for 48 h, the powder gradually turned bright yellow (δ-$FAPbI_3$). Then, the powder was washed with ACN at least five times. The final product was dried in a vacuum oven (40 ℃) for 3 d to remove any remaining solvent before baking at 140 ℃ for 5 h. The yellow $FAPbI_3$ powder gradually changed to black and formed a black α-phase $FAPbI_3$ (Fig. S1). The black powder was stored in an Ar filled glove box for later use. The $MAPbBr_3$ synthesis method was similar to that described above but with different raw materials: MABr (4.98 g) and $PbBr_2$ (14.08 g)

Synthesis of TiO_2 nanocrystals

The TiO_2 nanocrystals were synthesised following a modified non-hydrolytic sol-gel method with all procedures performed in ambient air.[2-4] First, 8 mL of $TiCl_4$ (99.9%, Sigma-Aldrich) was injected dropwise into 32 mL cold anhydrous ethanol (in an ice bath) with strong stirring to avoid local overheating of ethanol. After the solution cooled to room temperature, 160 mL of anhydrous benzyl alcohol was added and the mixture was stirred for 20 min. The original yellow solution became reddish after the addition of benzyl alcohol. The mixed solution was then transferred into a 250-mL firmly sealed glass bottle and stored without stirring in an oven at 85 °C for 9 h, during which time a slightly milky suspension of TiO_2 formed (Fig. S2). The product TiO_2 nanocrystals were then precipitated from the as-obtained solution by the addition of 800 mL diethyl ether and isolated by centrifugation at 8000 rpm for 10 min. The solid was subsequently washed by adding anhydrous ethanol and diethyl ether, followed by a similar centrifugation step (8000 rpm for 5 min). The as-obtained product was re-dissolved in 80 mL absolute ethanol and precipitate with the addition of 250 mL diethyl ether; this procedure was repeated three times. The obtained TiO_2 nanocrystals were collected and dispersed in mixed solution methanol/ethanol (1:1, V/V) to make a suspension with a concentration of around 8 mg/mL. To stabilise the as-obtained TiO_2 nanocrystals solution, titanium diisopropoxide bis(acetylacetonate) (TiAcAc; 2 μL/mg) was added; the obtained solution was transparent and showed a slight yellow colouration.

Device Fabrication

Unit device fabrication

For the unit solar cell (2 cm × 2 cm), the pre-patterned FTO substrates were cleaned by sonication with deionised water, ethanol, and acetone for 15 min each. After drying under a N_2 stream, the substrates were cleaned by ultraviolet (UV)/ozone treatment for 30 min. The as-prepared TiO_2 nanocrystals were deposited at a rate of 3000 rpm (acceleration 3000 rpm/s), followed by annealing at 150 ℃ for 45 min. The pristine $FAPbI_3$ device was made by dissolving 1032 mg of $FAPbI_3$ black powder (with 39 mg MACl used as an additive); the $(FAPbI_3)_{0.95}(MAPbBr_3)_{0.05}$ (FAMA) device was made using 980 mg $FAPbI_3$ and 39 mg $MAPbBr_3$ (with 36 mg MACl used as an additive); for the FASCl-doped device, 1032 mg synthesised $FAPbI_3$ black powder was doped with x mol.% FASCl (x = 0, 2, 4, 6 mol.%), with all perovskites dissolved in a 1 mL mixed solvent (DMF 700 μL, DMSO 300 μL). For each sample, 40 μL of the filtered perovskite precursor solution was spread on the TiO_2/FTO layer at 5000 rpm for 25 s; 0.55 mL of anisole was dropped on after 18–20 s, followed by annealing at 150 ℃ for 15 min.

After the substrate cooled to room temperature, 100 μL of phenylethylammonium iodide (PEAI; 5 mg/mL dissolved in a mixed solvent of isopropyl alcohol [150 μL] and toluene [850 μL]) or oleylammonium iodide (5 mg/mL, dissolved in toluene) was spin-coated on the perovskite layer at 5000 rpm for 30 s. The hole transfer materials were deposited by preparing Spiro-OMeTAD in chlorobenzene (90 mg/mL) and mixing with 39 μL 4-tertbutylpyridine (tBP), 23 μL Li-TFSI (520 mg/ mL in acetonitrile), and 10 μL tris[2-(1H-pyrazol1-yl)-4-tert-butylpyridine]-cobalt(III)-tris[bis-(trifluoromethylsulfonyl)imide] (FK209, great solar cell; 375 mg/mL–1 acetonitrile). PTAA was used instead of spiro-OMeTAD for thermal and moisture stability tests; the PTAA solution (20 mg/mL in toluene) was doped with 10 μL of Li-TFSI (350 mg/ml in acetonitrile) and 15 μL of 4-tertbutylpyridine. Then, 40 μL of PTAA stock solution was spin-coated on the as-prepared perovskite film at 4,000 rpm for 25 s. Finally, a 60 nm gold electrode was deposited on the substrate using a thermal evaporation system.

Mini module fabrication

An aperture area of 25.74 cm^2 in perovskite solar mini-modules, with a certain number of sub-cells (seven, eight, or ten) connected in series, was fabricated on the FTO glass substrates with a size of 7 × 7 cm^2. (8 × 8 cm^2 module with 12 sub-cells coated on a FTO glass substrates with a size of 10 × 10 cm^2). The series interconnection of the module was realised by P1, P2, and P3 lines, which were patterned using a laser etching system with a 1080 nm laser (μ-Lab, Germany; Fig. S26). The FTO glass was pre-patterned for P1 by means of 70% laser power with a frequency of 100 kHz and pulse width of 10 μs. The P1-patterned FTO glass was cleaned using the same method as that for the unit cells, which was followed by depositing the 40–50 nm TiO_2 layer, the perovskite film (~550 nm), PEAI or OLMI passivation layer (~10 nm), and the spiro-MeOTAD (~150 nm) layer sequentially on the prepared substrate using the spin-coating method. The P2 lines were patterned before Au deposition with an average laser power of 11%. Then, a 60 nm Au layer was deposited, and the P3 (11% power) line was formed. At the same time, both sides were etched for isolation between sub-cells. The P1, P2, and P3 scribes were all 100 μm in length. The distances between the P1 and P2 scribes and between the P2 and P3 scribes were 100–150 μm. The module design details are shown in Fig. S20.

DFT Calculation details

Geometry optimisation and electronic structure calculations

Density functional theory (DFT) calculations were performed using the VASP (Vienna ab-initio Simulation Package) code[5,6] employing the generalised gradient approximation with the Perdew-Burke-Ernzerhof scheme (GGA-PBE).[7] The projector-augmented wave (PAW) method with a 520 eV cut-off energy was used,[8] and the Van der Waals interaction was included using the DFT-D3 method.[9] For the modelling of the FASCl-doped $FAPbI_3$ with iodine vacancy, the (3 × 3 × 3) supercell made from $FAPbI_3$ pseudo-cubic unit cells containing 324 atoms was used. The charged supercells were achieved by adding or removing the electron from the neutral supercell with a vacancy. Atomic structures were relaxed until the calculated force on atoms was lower than 0.02 eV/Å; electronic step convergence thresholds were set to 10^{-5} eV, and a 2 × 2 × 2 Monkhorst–Pack k-point grid was used. In electronic structure calculations, the electronic step convergence threshold was set to 10^{-6} eV and a 4 × 4 × 4 Monkhorst–Pack k-point grid was used.

Formation energy calculation

Formation energy of FASCl-doped structures

The formation energies for pristine $FAPbI_3$ and FASCl-doped $FAPbI_3$ from the precursor were calculated according to the following equations (1–2):

$$E_f^{FAPbI_3} = \frac{1}{27}\left(27E^{FAPbI_3} - 27E^{FAI} - 27E^{PbI_2}\right) \tag{1}$$

$$E_f^{*} = E^{*} + (0.074 - 0.037x)E^{FACl} - (1 - 0.037x)E^{FAI} - E^{PbI_2} - 0.037E^{FASCl}, \tag{2}$$

where * is $FA_{0.926}FAS_{0.037}PbI_{3-0.037x}Cl_{0.037x}$; $E_f^{FAPbI_3}$ and $E_f^{doped\,FAPbI_3}$ are the formation energies of pristine $FAPbI_3$ and the FASCl-doped $FAPbI_3$, respectively; E^{FAPbI_3}, $E^{doped\,FAPbI_3}$, E^{FAI}, E^{FACl}, E^{PbI_2}, and E^{FASCl} are DFT-calculated total energies of each compound; and x is 0, 1, or 2 depending on the number of Cl^- ions doped in the $FAPbI_3$. The structures of FAI and FASCl were as previously reported, and the structure of FACl was obtained by replacing the I of FAI with Cl.[10, 11]

Formation energy of the iodine vacancy

The iodine vacancy formation energy ($E_f(V_I)$) depending on the Fermi energy was calculated using equation (3):

$$E_f(V_I) = E_{defected} - E_{perfect} + \mu_I, \quad (3)$$

where $E_f(V_I)$ is the iodine vacancy formation energy; $E_{defected}$ and $E_{perfect}$ are the DFT-calculated total energies for the FAPbI$_3$ with an iodine vacancy and for the perfect FAPbI$_3$, respectively; and μ_I is the chemical potential of iodine. Here, $\frac{1}{2}\mu_{I_2}(bulk)$ was used, assuming an iodine-rich condition.

Device characterisation

The current–voltage characteristics of the solar cells were measured using a solar simulator (Newport Oriel Solar 3A Class AAA, 64023A) and a potentiostat (CHI 660D, CH instruments); measurements were conducted under AM 1.5 G spectrum (100 mA cm^{-2}) illumination, and the potentiostat was calibrated using a standard Si-solar cell (Oriel, VLSI standards) and a light sensor current controller (Newport Oriel digital exposure controller, Model 68945). All devices were measured by masking the active area with a thin mask (0.14 cm^2). Except specially illustration, all *J–V* curves were measured in reverse (1.2 to −0.1 V; RS) or forward scan (−0.1 to 1.2 V; FS) with a scan rate of 200 mV s^{-1} under simulated AM 1.5G one sun illumination (100 mW cm^{-2}) in ambient air, (room temperature and humidity controlled at 5–10%). We typically performed light-soaking of the devices under one sun conditions for 20–30 s before starting *J–V* measurements. The module *J–V* cures were measured under the same environment conditions; the scan range change from reverse (9.5 to −0.1 V) to forward (−0.1 to 9.5 V) with a scan rate of 800 mV s^{-1} (for 10 sub-cells over 25.74 cm^2 or 12 sub-cells over 65.22 cm^2, the scan voltage changed from 12 to 14 V, respectively). The liquid state ^{1}H nuclear magnetic resonance (NMR) measurements were recorded on a Bruker AVANCEⅢ700 700 MHz spectrometer. Steady-state photoluminescence (SSPL) spectra were measured using a fluorescence lifetime spectrometer (Quantaurus Tau C11367-12, HAMAMATSU) with excitation by a 464 nm laser (PLP-10, HAMAMATSU) pulsed at a frequency of 10 MHz. TPV and TPC measurements were performed using a nanosecond laser (10 Hz, NT342A, EKSPLA) as a small-perturbation light source and a Xe lamp (300 W, Newport) as a bias light source. The device was directly connected to a digital oscilloscope (350 MHz, MDO4034C, Tektronix), whose input impedance was set to 1 MΩ for TPV and 50 Ω for TPC. The bias light intensity was controlled by neutral density filters for various open-circuit voltages (V_{oc}). A strongly attenuated laser pulse (550 nm) was used to generate a transient voltage (ΔV) of less than 20 mV. TRPL was detected using the time-correlated single-photon counting system (PicoQuant, PicoHarp 300 with LDH-P-C-670) to measure spontaneous PL decay. Scanning electron microscopy (SEM) images and elemental contents were obtained using a JSM-7600F hot field emission scanning electron microscope (JEOL, Japan). EIS measurements were obtained using an Autolab 302B under dark conditions in a frequency range from 1 to 100 Hz. The capacitance–voltage (*C*–*V*) curve was plotted for Mott-Schottky analysis using an impedance spectroscope (VMP3, Bio-logic science instruments) with a frequency of 10 kHz under dark conditions. The X-ray diffraction patterns of the perovskite films were measured using a D8 Discover instrument with Cu Kα radiation ($\lambda = 1.5418$ Å). UV–visible (vis) spectra were measured using a UV–vis spectrometer (Lambda 45, Perkin Elmer), and the UV–vis spectrum of the perovskite film on the FTO substrate was measured. X-ray photoelectron spectra (XPS) were collected using an ESCALAB 250 XPS system (Thermo Fisher Scientific) with Al Kα X-ray radiation (1486.6 eV). The IPCE spectral measurements were obtained using an IPCE system (photovoltaic measurements) in DC mode, where the monochromatic beam was supplied with a 75 W Xe lamp (USHIO). Impedance spectra were measured in the dark using an Autolab 302B in the frequency range of 0.1–1 MHz.

Supplementary Figures

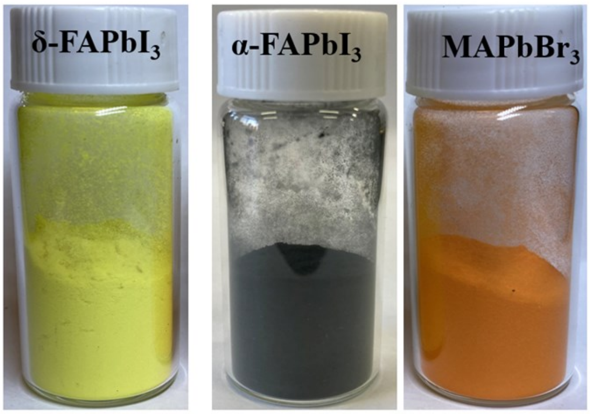

Figure S1. Pictures of synthesized yellow δ-$FAPbI_3$, black α-$FAPbI_3$, and $MAPbBr_3$ powders

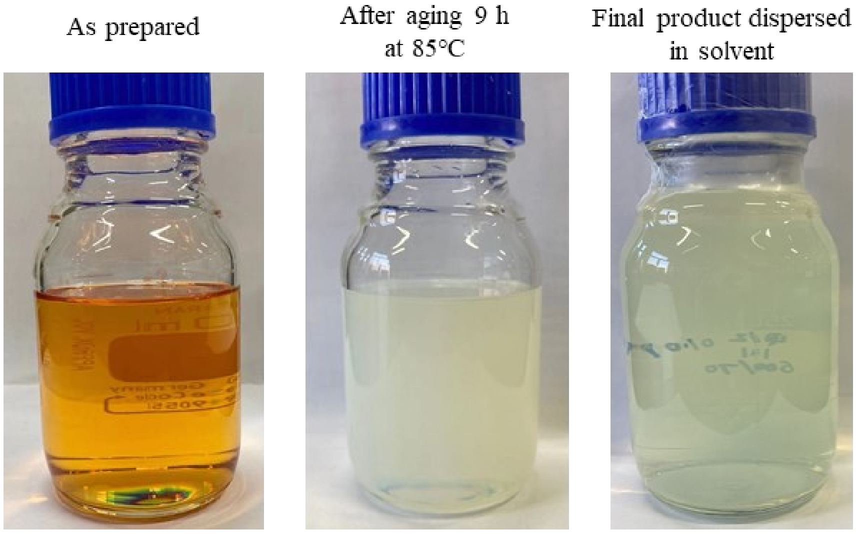

As prepared

After aging 9 h at 85°C

Final product dispersed in solvent

Figure S2. Pictures of synthesized TiO_2 nanocrystal.

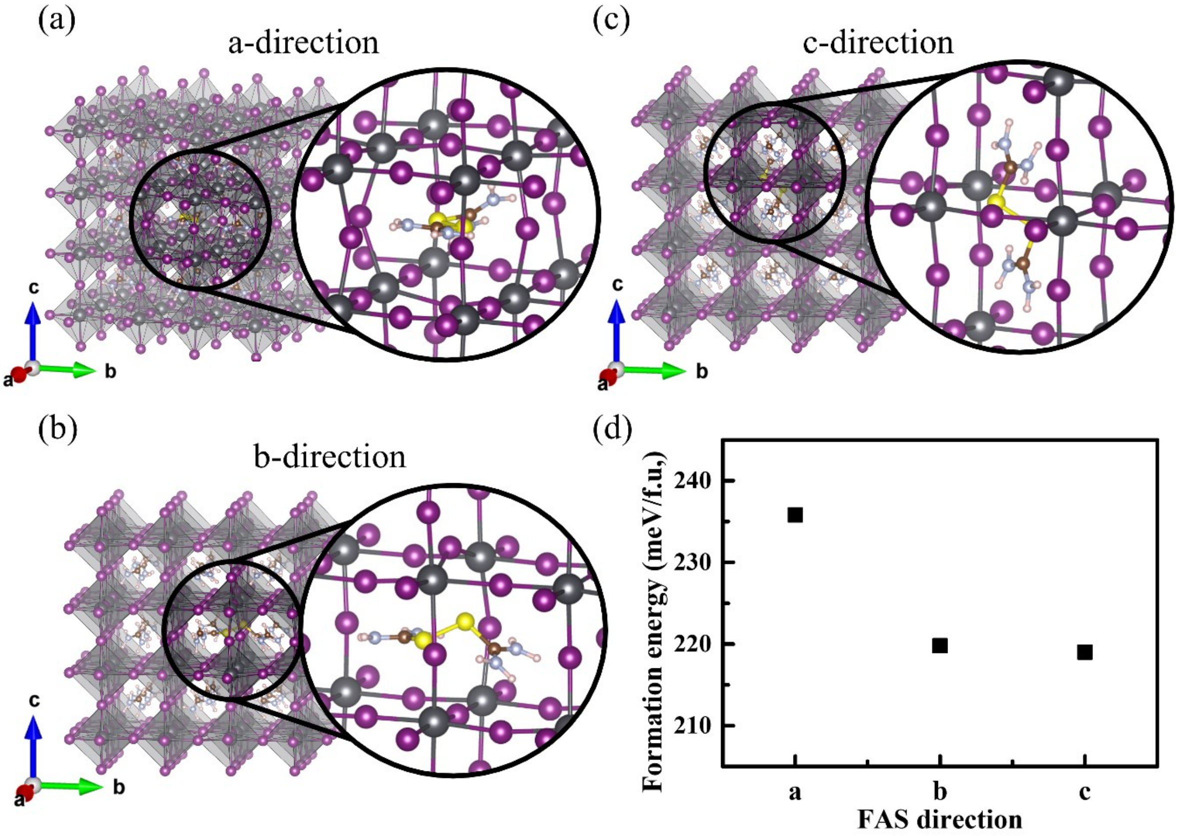

Figure S3. Optimised atomic structure of $FA_{0.926}FAS_{0.037}PbI_3$ according to the direction of the FAS^{2+} in the $FAPbI_3$ along the a direction (a), b direction (b), and c direction (c). (d) Formation energies of each structure.

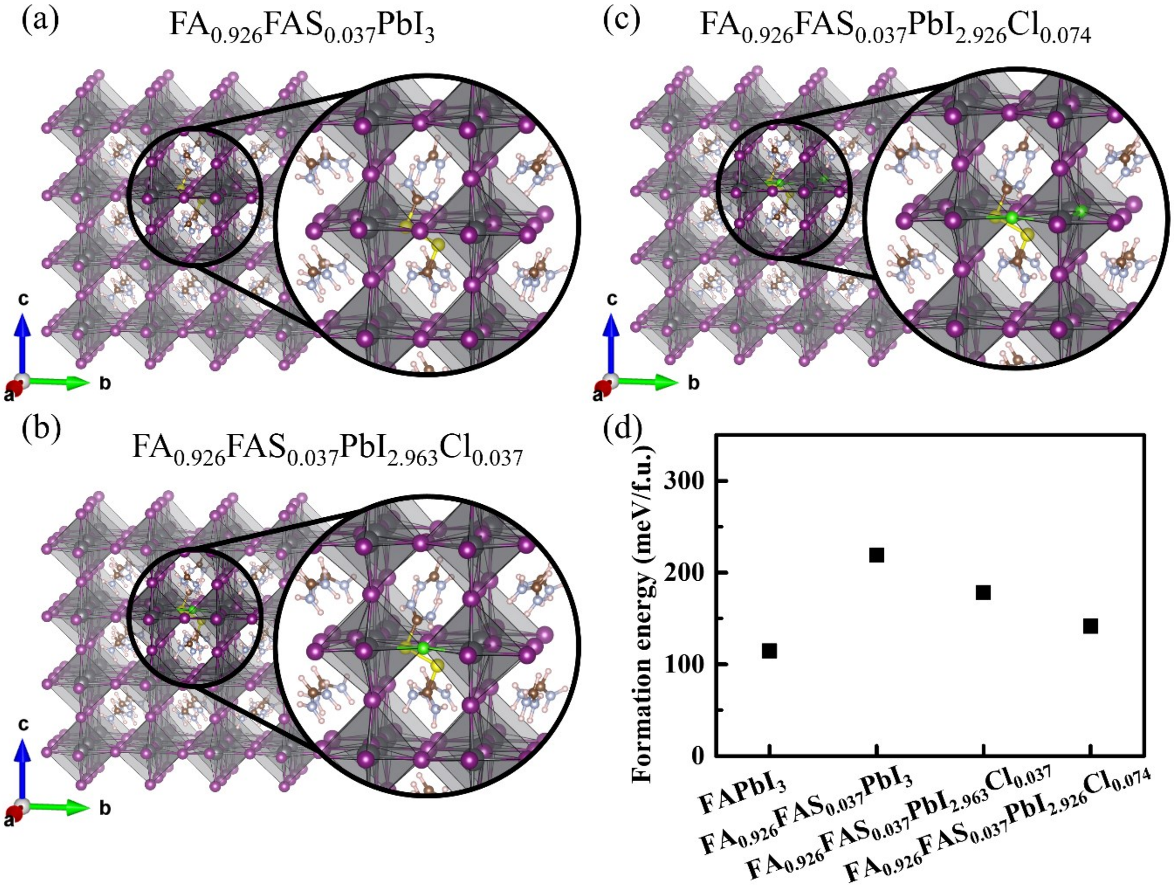

Figure S4. Optimised atomic structures of (a) $FA_{0.926}FAS_{0.037}PbI_3$, (b) $FA_{0.926}FAS_{0.037}PbI_{2.963}Cl_{0.037,}$ and (c) $FA_{0.926}FAS_{0.037}PbI_{2.926}Cl_{0.074}$. Numbers of co-doped Cl^- in the $FAPbI_3$ supercells are 0, 1, and 2 for (a), (b), and (c), respectively. (d) Formation energy of each structure.

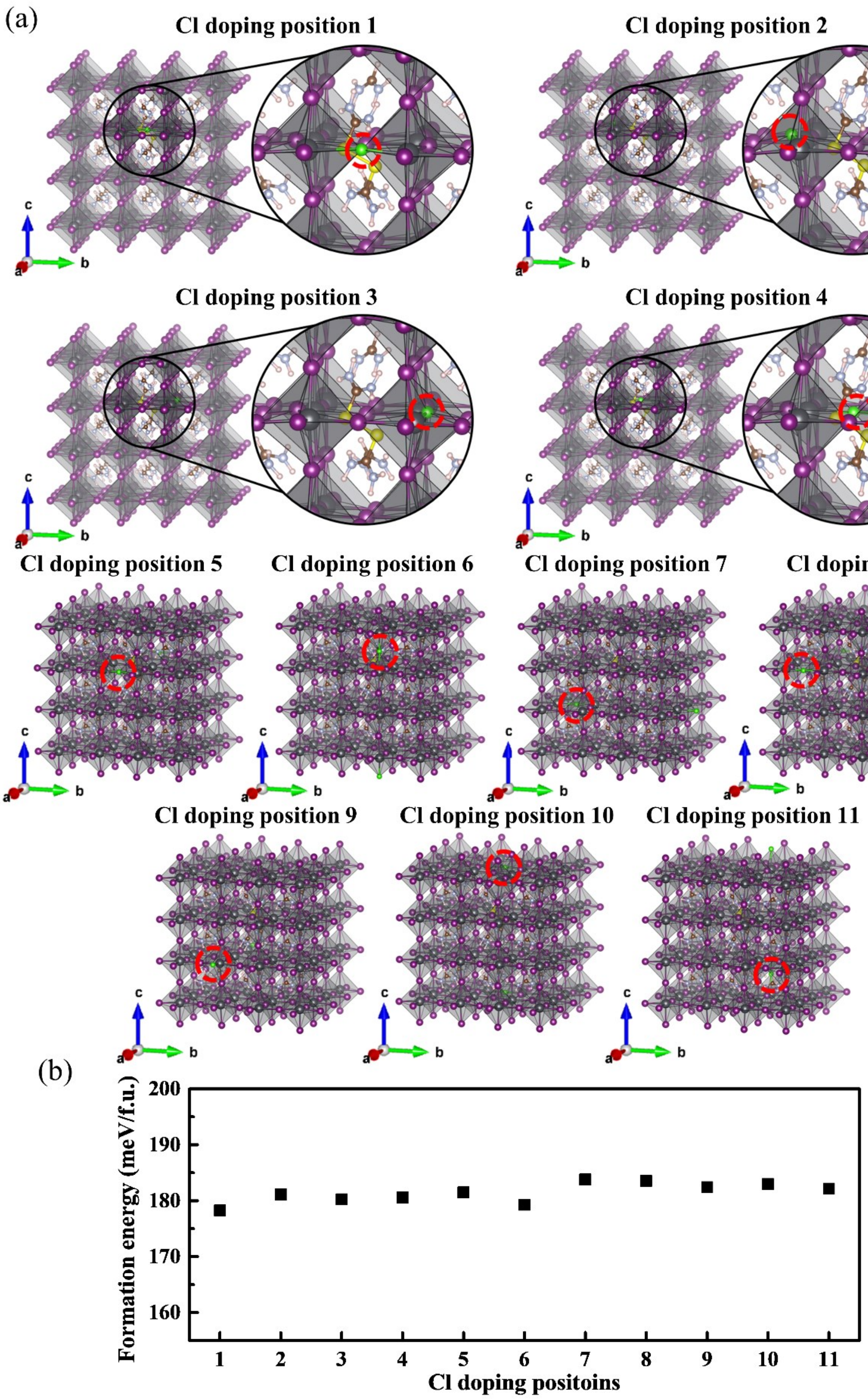

Figure S5. (a) Relaxed atomic structure of FA$_{0.926}$FAS$_{0.037}$PbI$_{2.963}$Cl$_{0.037}$ according to the position of the Cl$^-$ ion. (b) Formation energies of each atomic structure. Light green spheres in the red circles represent Cl^- ions. Cl^- doping positions 1–4 show structures where Cl^- ions substitute I^- ions neighbouring S atoms in doped FAS^{2+}; Cl^- doping positions 5–11 show structures where Cl^- ions substitute I^- ions randomly regardless of FAS^{2+} position.

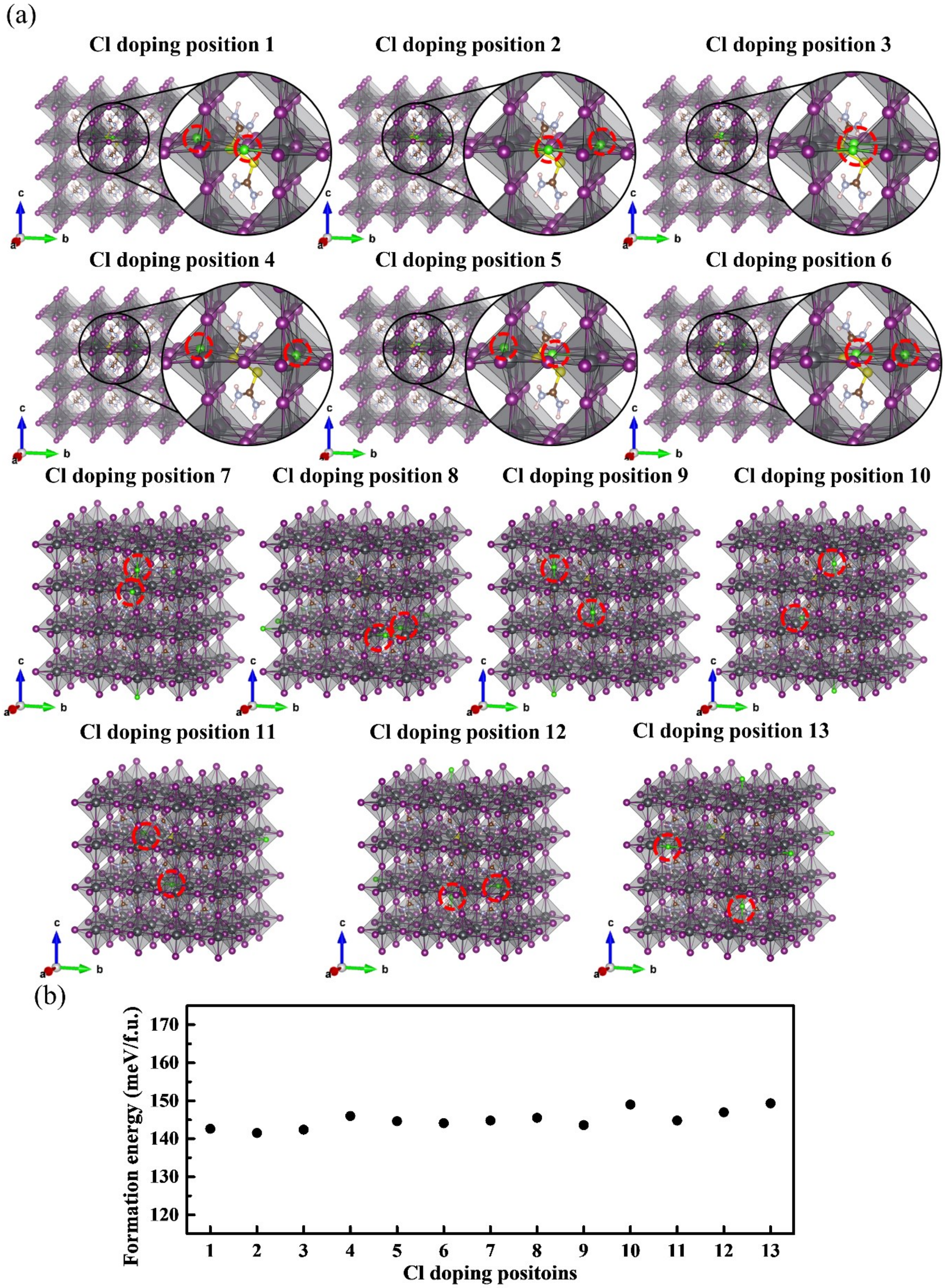

Cl doping position 1

Cl doping position 2

Cl doping position 3

Cl doping position 4

Cl doping position 5

Cl doping position 6

Cl doping position 7

Cl doping position 8

Cl doping position 9

Cl doping position 10

Cl doping position 11

Cl doping position 12

Cl doping position 13

Figure S6. (a) Relaxed atomic structure of $FA_{0.926}FAS_{0.037}PbI_{2.926}Cl_{0.074}$ according to the position of the Cl^{-} ion. (b) Formation energy of each atomic structure. Light green spheres in red circles represent Cl^- ions. Cl^- doping positions 1–6 show structures where Cl^- ions substitute I^- ions neighbouring S atoms in doped FAS^{2+}; Cl^- doping positions 7–13 show structures where Cl^- ions substitute I^- ions randomly regardless of FAS^{2+} position.

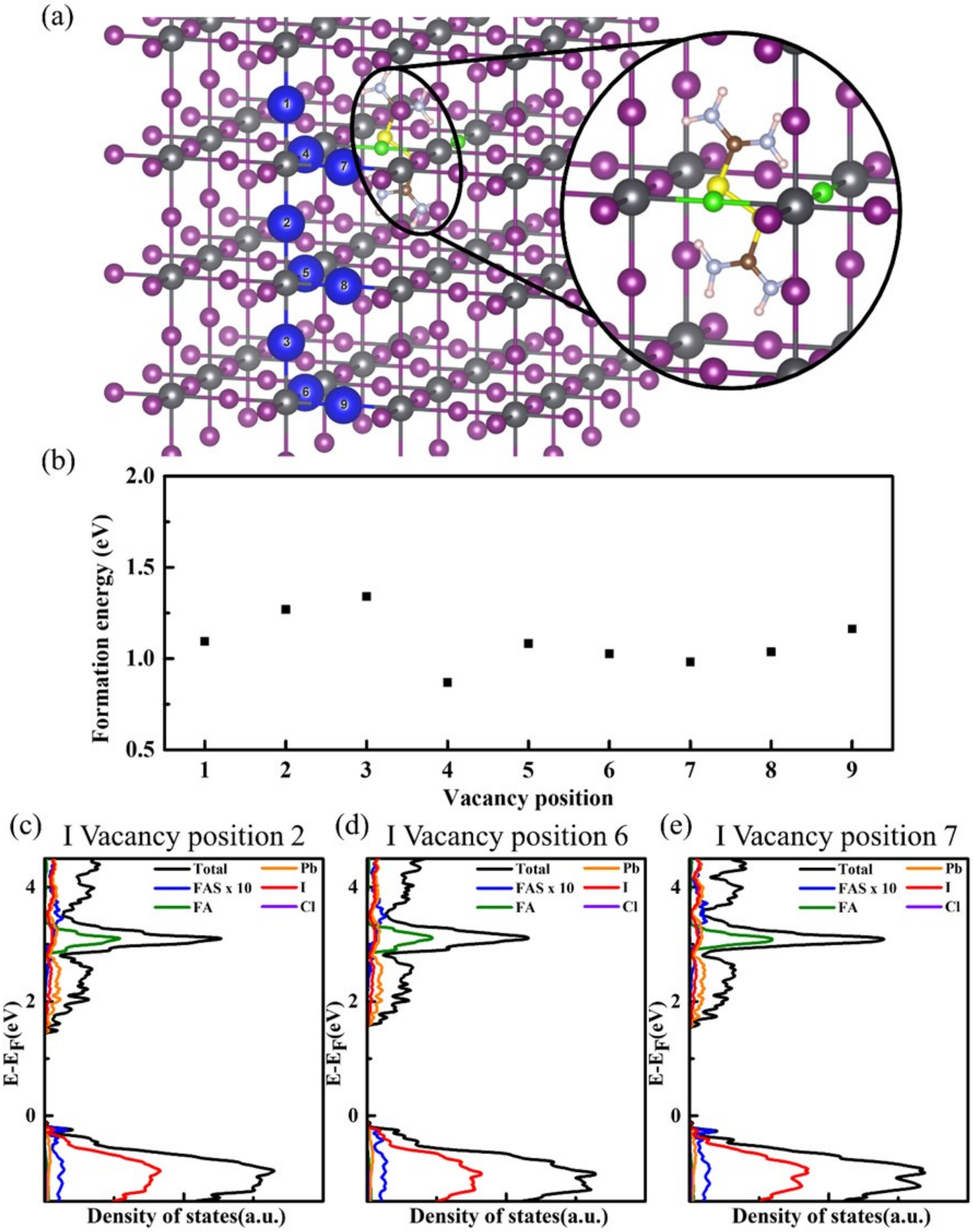

Figure S7. (a) Schematic figure of the iodine vacancy position in FASCl-doped $FAPbI_3$ considered in the density functional theory (DFT) calculation. Iodine vacancy site is shown by blue spheres and numbers. (b) Formation energy of the iodine vacancy depending on position; formation energy of the iodine vacancy in pristine $FAPbI_3$ is represented in red. (c–e) Densities of state for the iodine vacancy when located at each position.

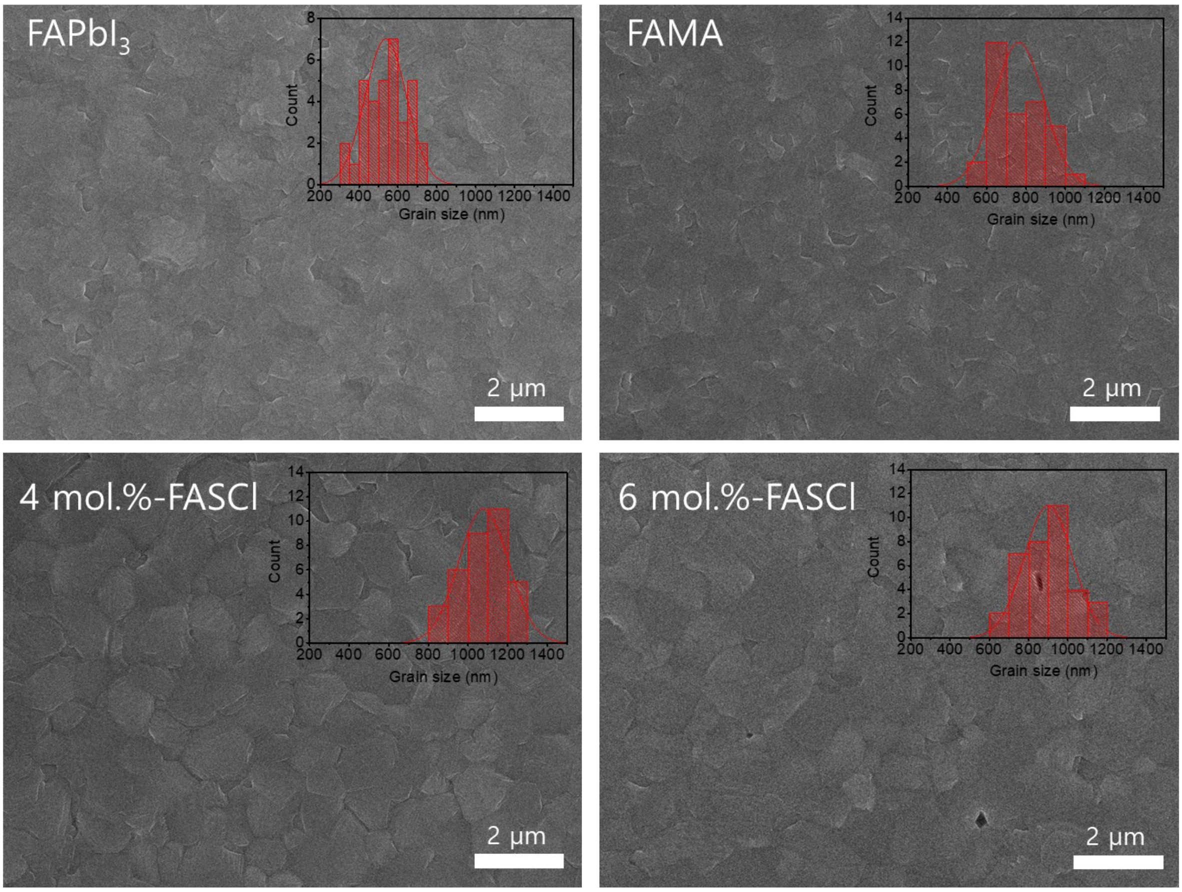

Figure S8. Scanning electron microscope (SEM) images of the surface $FAPbI_3$ perovskite films doped with different additives. Grain size distributions estimated from the SEM images using Nano measurer 1.2 software (inset).

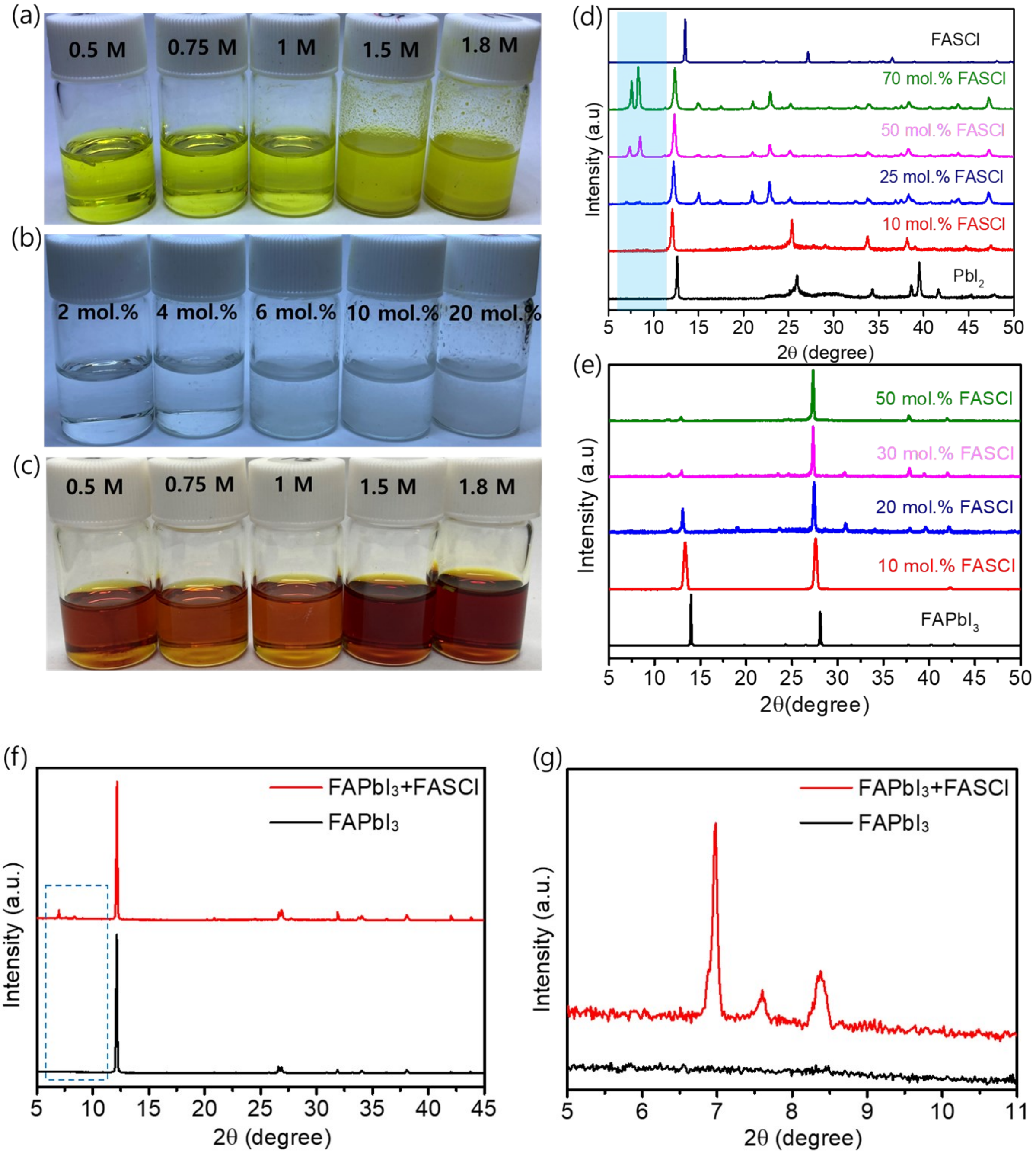

Figure S9. Photographs of different amounts of (a) PbI_2 and (b) FASCl dissolved in DMF. (c) Photograph of different amounts PbI_2 mixed with 10 mol.% FASCl dissolved in DMF. (d) X-ray diffraction (XRD) patterns of the 1.6 M PbI_2 film with doped different amounts of FASCl additive coated on glass substrates. (e) XRD patterns of $FA_{1-x}FAS_xPbI_3$ perovskite (x = 10, 20, 30 and 50 mol.% perovskite films coated on glass). (f) and (g) show the XRD patterns of the wet perovskite film with or without 4%mol of FASCl.

Note for Figure S9. We added different amounts PbI_2 or FASCl into DMF solution and studied their solubilities in DMF. As shown in Fig. S9a, PbI_6 octahedral colloids are prone to precipitate in the DMF solution owing to the formation of one-dimensional PbI_2-DMF-contained solvate phases (PDS), which limits the solubility of PbI_2 in the DMF solution (~1.0 M).[12, 13] We also found that small amounts of FASCl (≤ 4 mol.%) can be readily dissolved in DMF at room temperature after shaking the solution for 2–5 min (Fig. S9b). However, we can see that even 10 mol.% of FASCl is hard to fully dissolve in DMF; however, it easily dissolves after mixing with PbI_2 and a transparent crimson solution is formed after a few minutes of shaking at room temperature (Fig. S9c, notably, even 1.8 M PbI_2 can be dissolved into DMF after adding 10 mol.% FASCl). This can be explained by FAS^{2+} cations diffusing into PbI_2 to construct an intermediate phase of $x[FAS^{2+}]\cdot 2[PbI_2Cl_x]^{x-}$, which significantly promotes the dissolution of FSACl and PbI_2 in the DMF solvent and affects the crystal growth process. The interaction of FASCl and PbI_2 was also investigated using XRD; varying amount of (x mol.%) FASCl (x = 10, 25, 50, and 70) was added into 1.6 M PbI_2 (DMF used as solvent) as an additive. Films prepared for XRD testing were coated with a mixed solution on glass substrate at 2000 rpm for 30 s and annealed at 100 ℃ for 10 min. With increasing FASCl doping concentration in the PbI_2/DMF solution, two new XRD peaks appeared at 7.3° and 8.5°. In addition, the diffraction intensity was proportional to the FASCl doping amount (Fig. S9d), indicating a strong interaction between FASCl and PbI_2. This is in contrast to previous studies, where most of the divalent diammonium cations reported have been used to realise two dimensional (2D) or 2D/three-dimensional (3D) mixed structures, which contain the Dion–Jacobson phase.[14, 15] Although this improved the perovskite stability, these large organic diammonium cations act as insulating spacing layers between conductive inorganic slabs, inhibiting charge transport between neighbouring inorganic layers and deteriorating the performance of 2D/3D PSCs compared with 3D perovskite.[16] The $FA_{1-x}FAS_xPbI_3$ perovskite structure confirmed by XRD, even doped with 50 mol.% FASCl, does not show any 2D phase (Fig. S9e). To further confirm the intermediate phase in low concentration doping, we coated perovskite film with or without 4 mol.% of FASCl on FTO substrate. As shown in Fig. S9f and S9g, compare to pure $FAPbI_3$ wet film, the wet perovskite film contains 4% mol of FASCl shows the peak around 6.98, 7.61

and 8.36, which is assigned to the x$[FAS^{2+}]\cdot 2[PbI_2Cl_x]^{x-}$ intermediate phase. (The wet film prepared by dropped perovskite precursor solution on the FTO substrate, after treated by antisolvent (anisole), the wet film measured XRD immediately.)

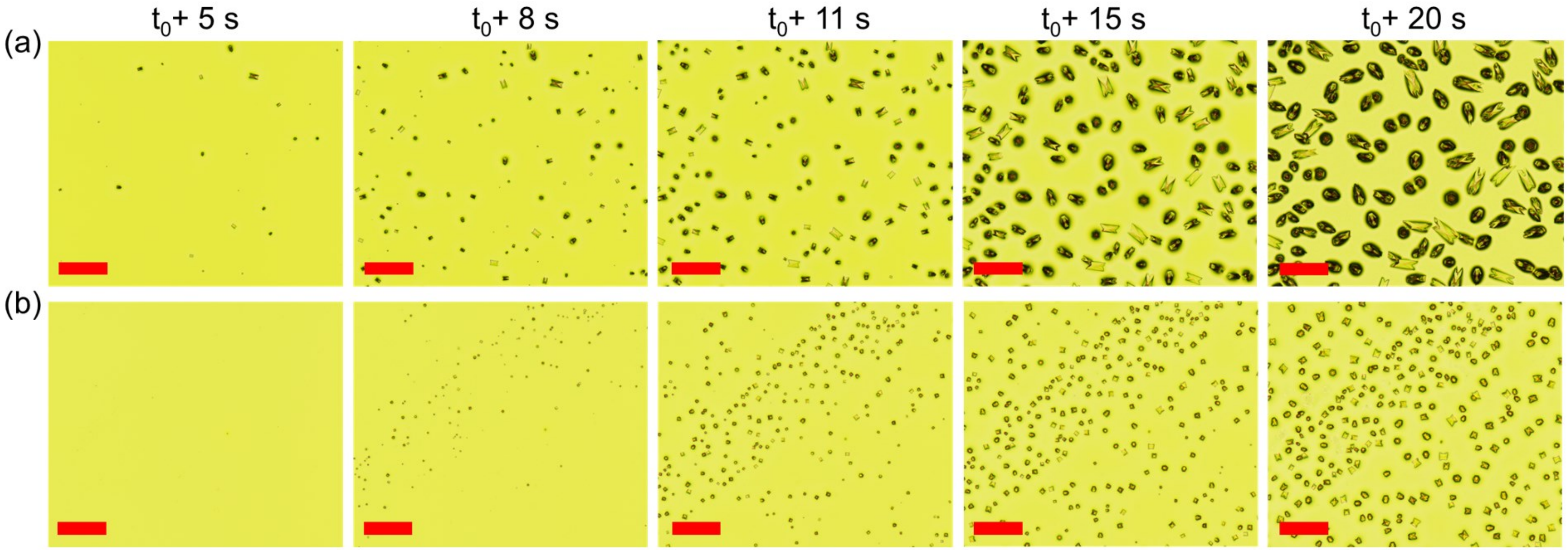

Figure S9-1. Optical microscopic images of the wet films observed as a function of time for the $FAPbI_3$ solution (a) without (pristine) or (b) with 4 mol.% FASCl doped. (The inset scale bar is 100 µm). All images were observed using an optical microscope (DS-Ri2, Nikon, Tokyo, Japan)

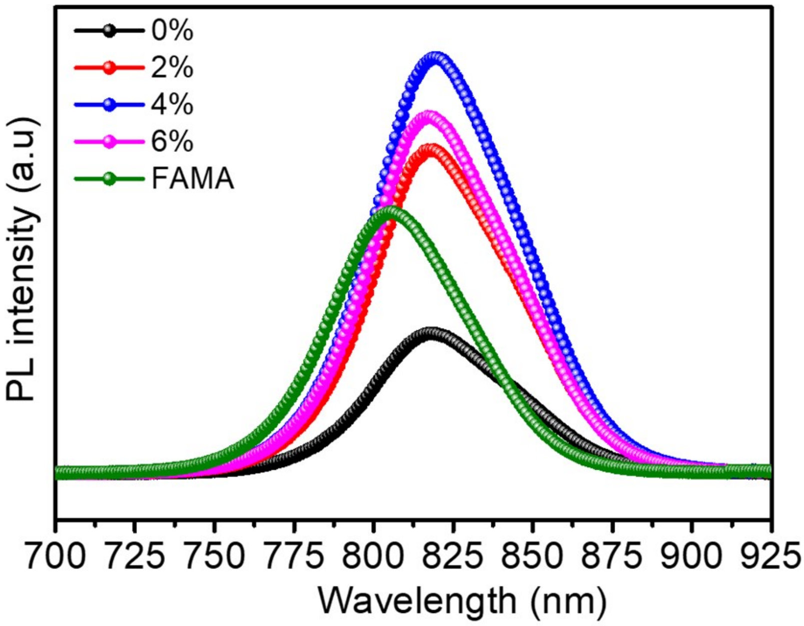

Figure S10. Steady-state Photoluminescence (SSPL) spectra for different x values of $FAPbI_3$:xFASCl (x = 0, 2, 4, and 6 mol.%) and the control.

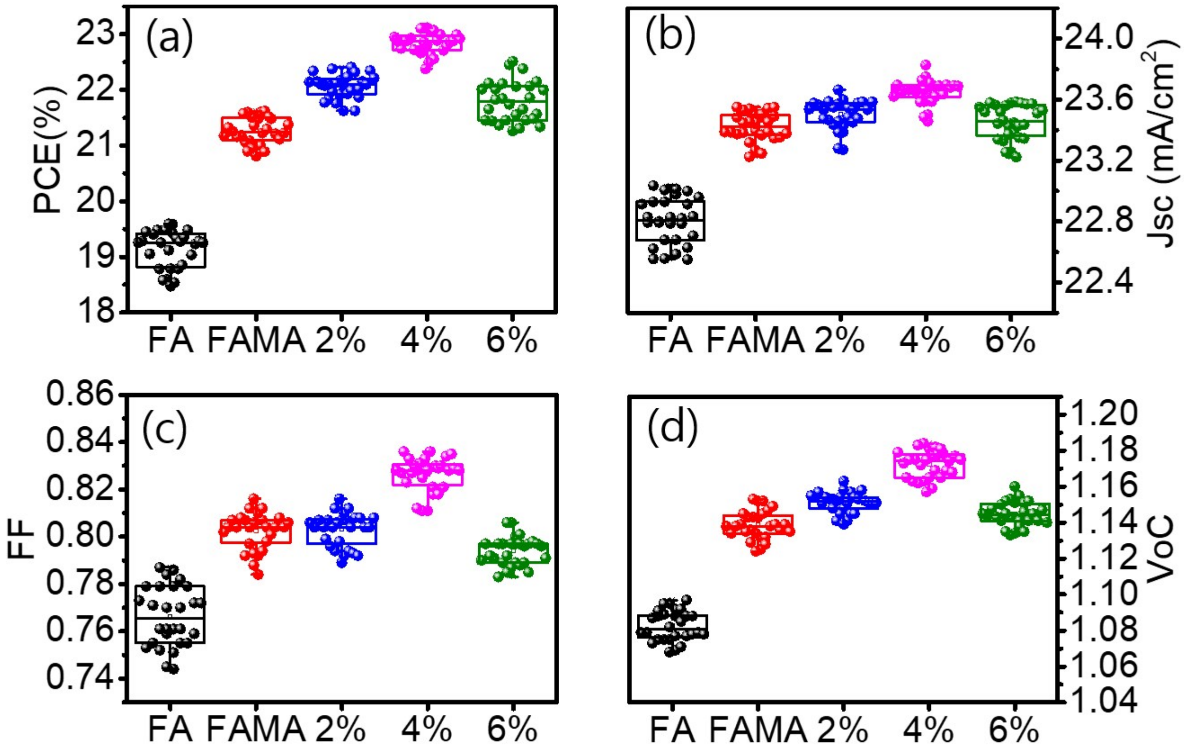

Figure S11. Statistics of photovoltage (PV) parameters for devices based on the pristine, control, and x mol.% of FASCl containing perovskites. Abbreviations: V_{oc}, open-circuit voltage; J_{sc}, short-circuit current density; FF, fill factor; PCE, power conversion efficiency.

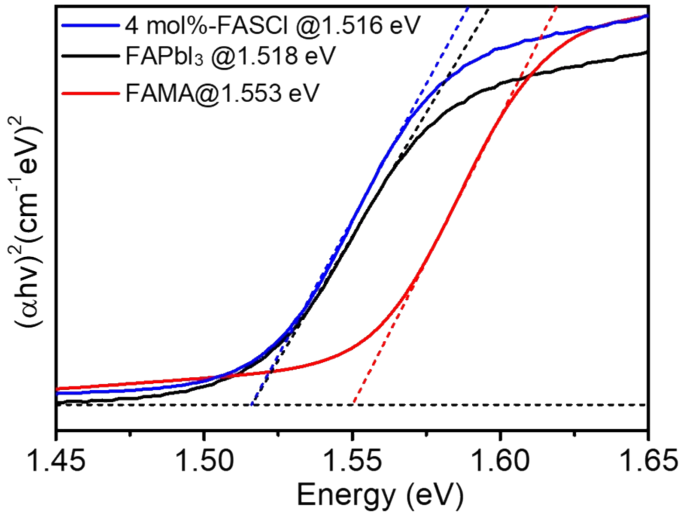

PVSK	Eg (eV)	Voc (V)	Voc loss (V)
$FAPbI_3$	**1.518**	**1.085**	**0.433**
FAMA	**1.553**	**1.147**	**0.406**
4 mol%-FASCl	**1.516**	**1.173**	**0.343**

Figure S12. Calculated band gap from ultraviolet–visible (UV–vis) absorption and corresponding voltage loss, where the open-circuit voltage (V_{oc}) loss is ($E_{abs}/q - V_{oc}$).

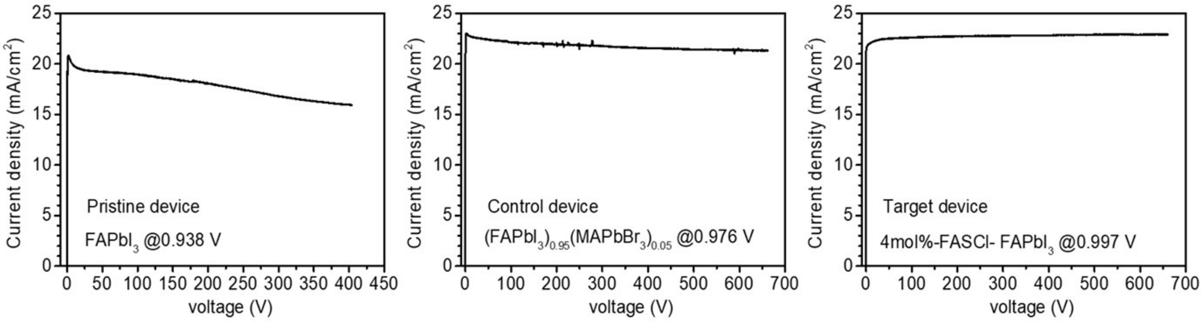

Figure S13. Stabilised output current density for pristine, control, and target perovskite solar cell devices around the maximum output power point under simulated 1 sun illumination.

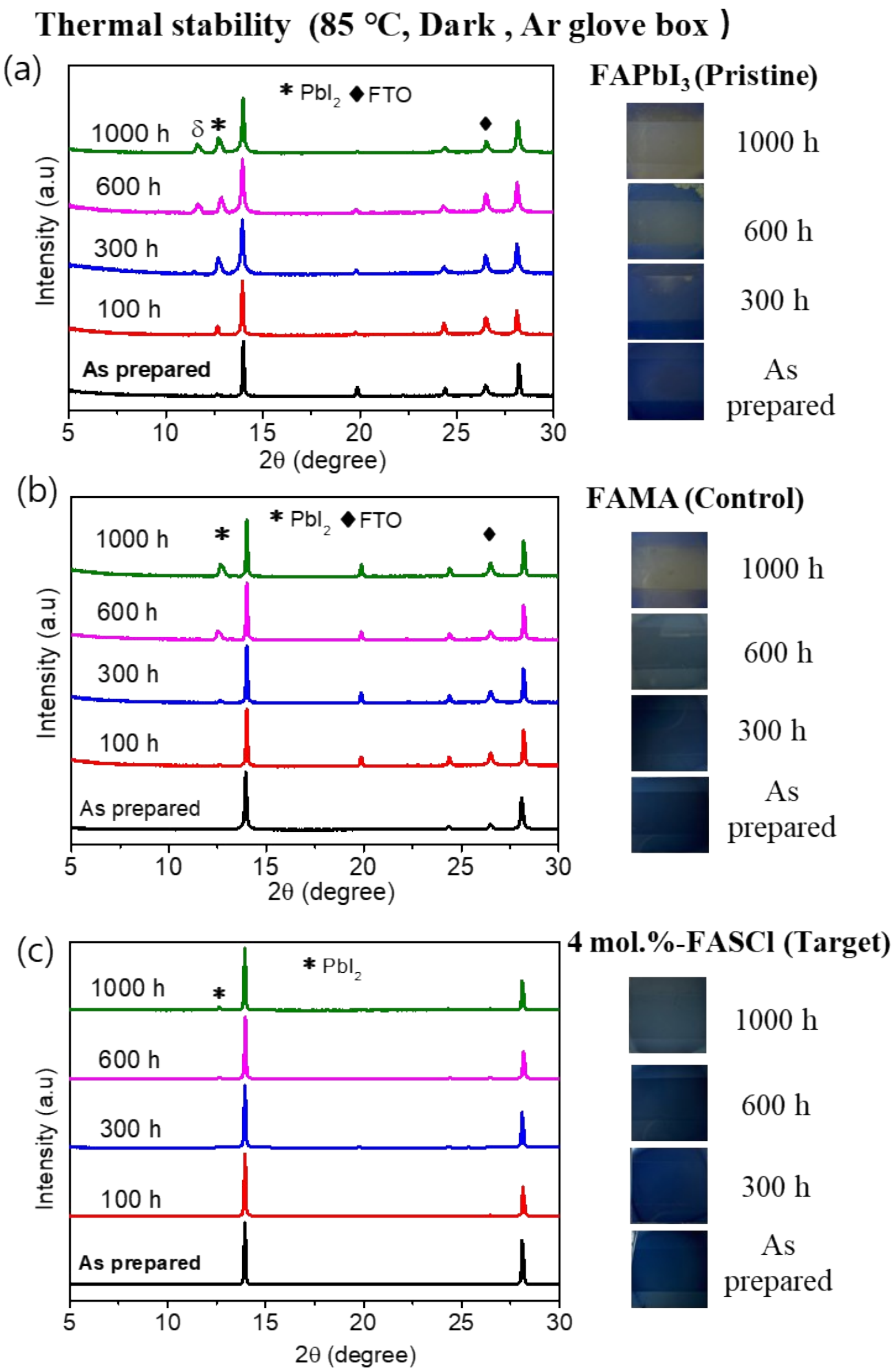

Figure S14. Stability tests of pristine (a), control (b), and target (c) perovskite films against thermal stress. The right-hand column shows images of corresponding film changes with ageing time.

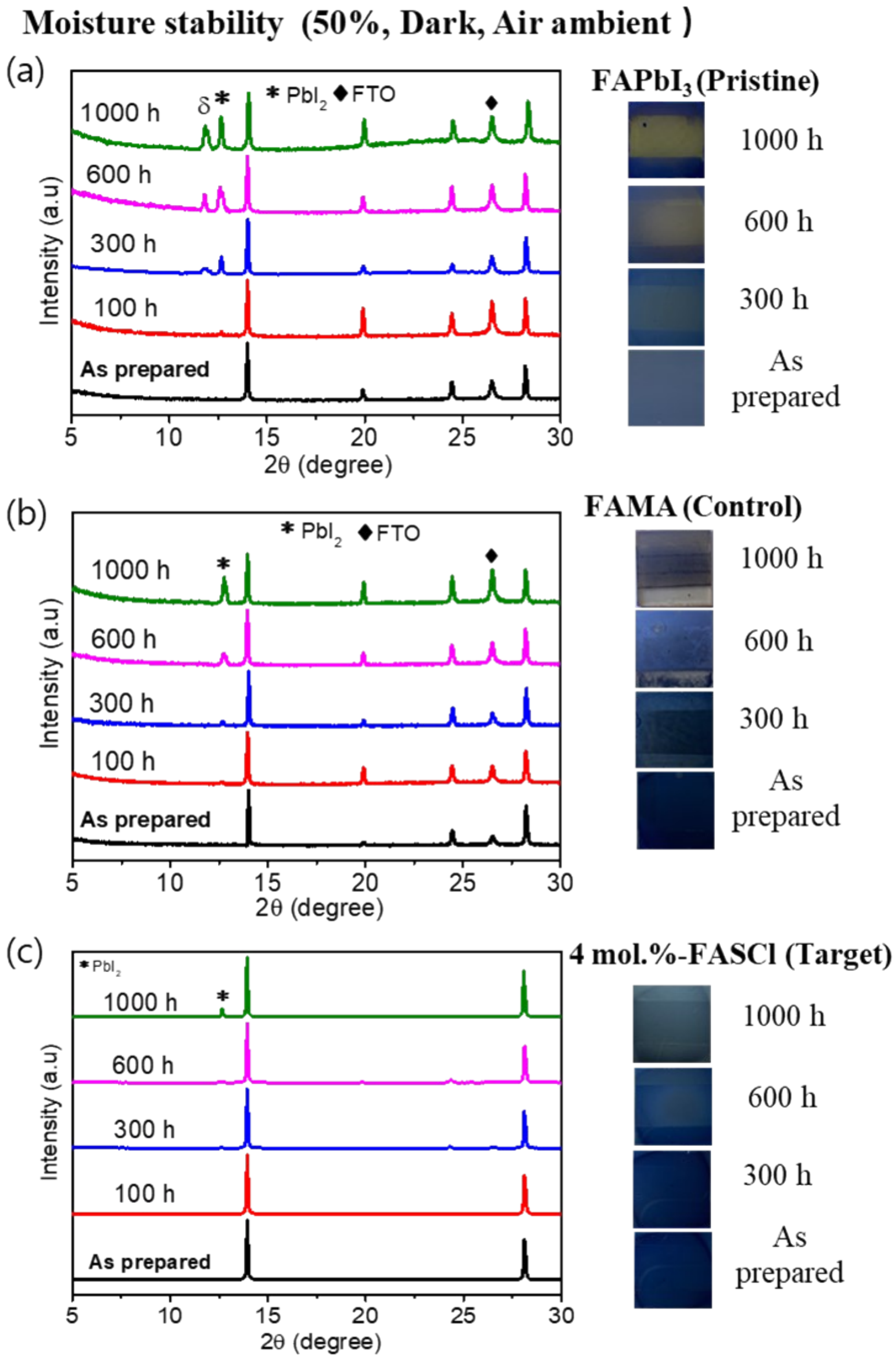

Figure S15. Stability test of the pristine (a), control (b), and target (c) perovskite films against moisture stress. Right-hand column shows images corresponding to film changes with ageing time.

Note for Figure S14 and Figure S15. The pure pristine $FAPbI_3$ perovskite film readily transformed from the desired trigonal black α-phase into the undesirable wide-bandgap δ-phase with hexagonal symmetry, even under ambient conditions at room temperature, this may lead to lower light harvest and charge transport efficiency.[17] For the thermal and humidity stability tests, the perovskite film was heated to 85 °C in an Ar atmosphere glove box or operated in an isolated commercial cabinet with 50% ± 5% relative humidity (RH) for 1000 h, respectively. Comparing the XRD results of the pristine, control, and FASCl-doped perovskite films for each of the two environmental stress tests, the pristine and control perovskite films showed peak intensity at approximately 12.5°. This highlights a significant increase and indicates the degradation of the PbI_2 in the perovskite. In particular, the pristine $FAPbI_3$ showed a yellow δ-phase at around 11.6°. In contrast, perovskite films doped with 4 mol.% FASCl presented a relatively low intensity of PbI_2 and without any yellow phase.

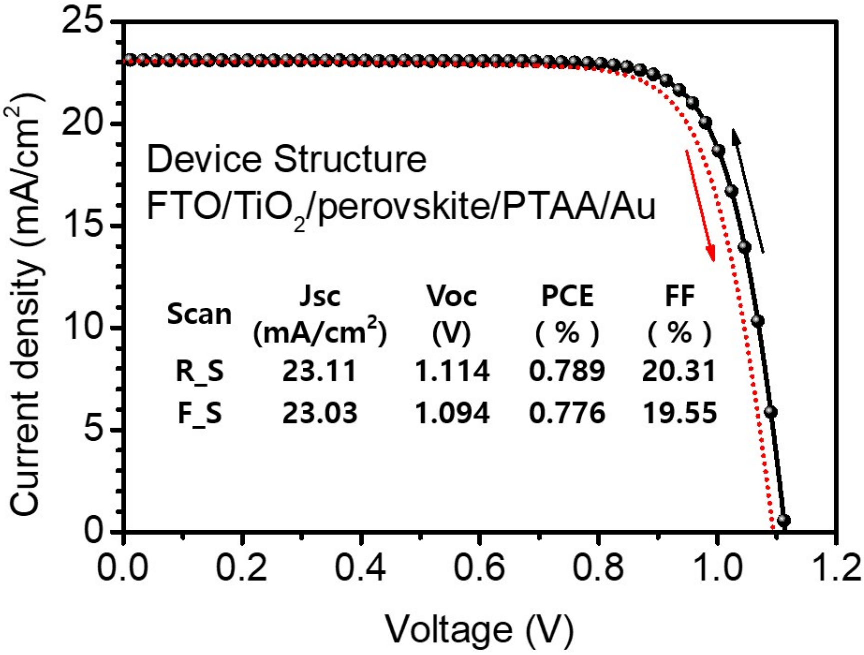

Scan	Jsc (mA/cm^2)	Voc (V)	PCE (%)	FF (%)
R_S	23.11	1.114	0.789	20.31
F_S	23.03	1.094	0.776	19.55

Figure S16. Initial current density–voltage (*J–V*) curves and photovoltage (PV) parameters of the target device with poly[bis (4-phenyl)(2,4,6-trimethylphenyl)amine] (PTAA) as a hole transport layer. Stability tests under humidity or thermal conditions were carried out with a device of the same structure. PTAA solution (20 mg/mL in toluene) was doped with 10 μL of Li-TFSI (350 mg/mL in acetonitrile) and 15 μL of 4-tertbutylpyridine.

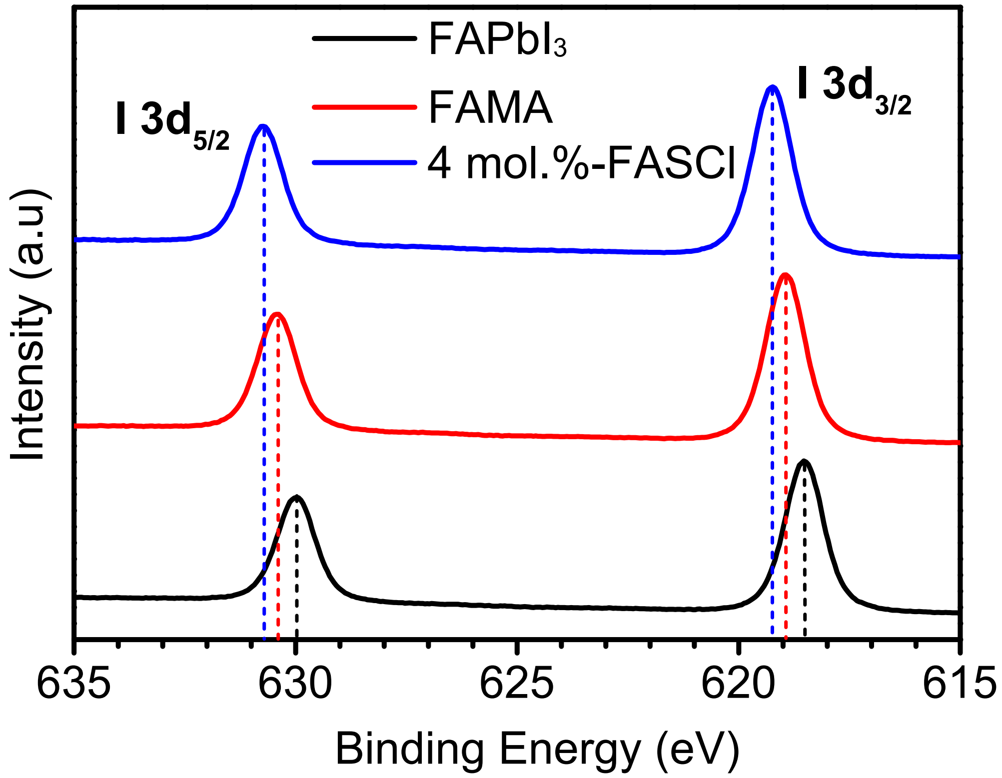

Figure S17. High resolution X-ray photoelectron spectra (XPS) spectra of iodine 3d for the pristine, control, and target perovskite films.

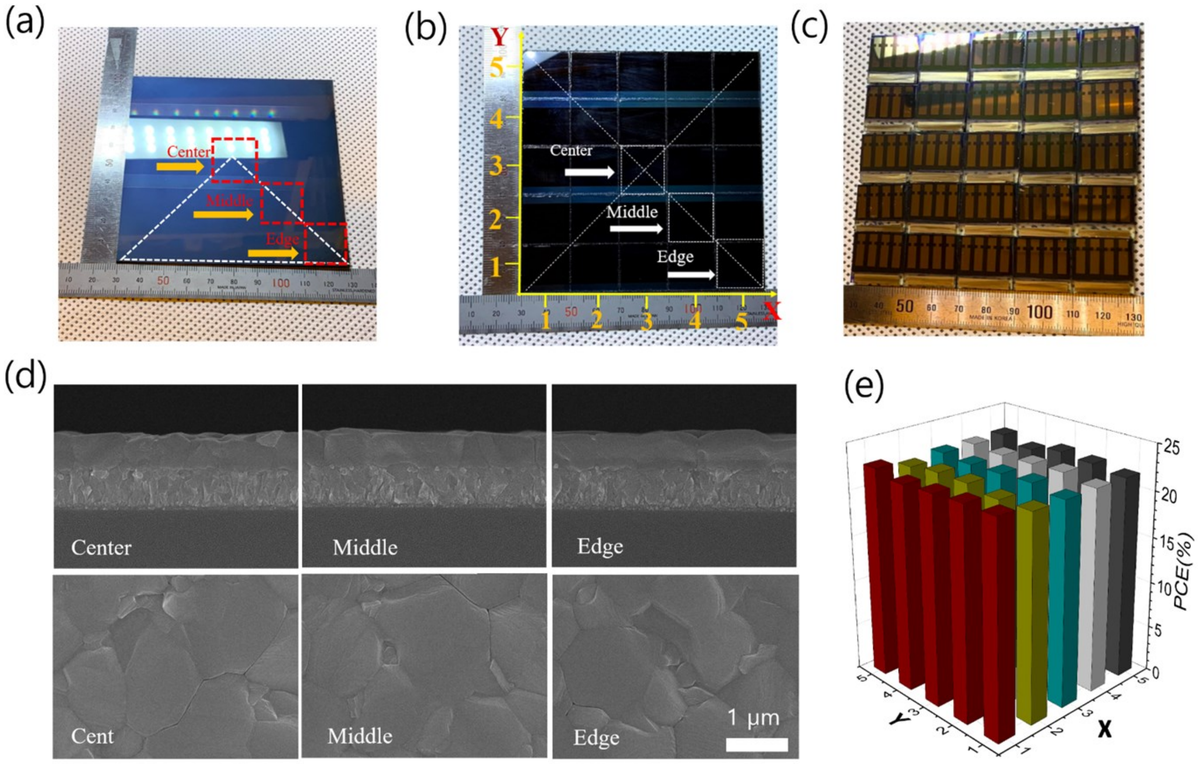

Figure S18. Photovoltaic performances of spin-coated large-area perovskite film prepared using 4 mol.% FASCl-doped $FAPbI_3$. (a) Front and back side (b) photographs of perovskite film coated on a TiO_2-coated fluorine-doped tin oxide (FTO) substrate (10 cm wide and 10 cm long). (c) After spin coating, the substrate was divided into 25 pieces to make perovskite solar cells (PSCs) with dimension of 2×2 cm^2. (d) Surface and cross section SEM images of the centre, middle, and edges of the devices (see 'figure S18a' for locations). (e) Power conversion efficiency (PCE) distribution of the best-performing PSC in each divided device.

Note for Figure S18. Fabrication of a uniform and pin-hole-free large-area perovskite film is a prerequisite for realising high efficiency perovskite modules. We tested the uniformity of the spin-coating method on a large-scale by using a pre-cut TiO_2-coated 10×10 cm^2 FTO glass substrate. As shown in Figure S18-1, for 10×10 cm^2 large area device coating, a large sized (diameter 5 cm) spin coater chuck is needed (1). Before coating, the 10×10 cm^2 substrate should be put in the centre of spin coater chuck to avoid any kind of machine damage during high-speed coting process (2). After fixed the substrate, 1 mL perovskite precursor solution dropped on it (3) and uniformly spread it the by a 5 mL pipette tip (4, 5). During the coating process, 5 mL antisolvent (anisole) dropped by a 5.5 mL pipette (a plastic cover used to avoid the solution random splash) (6, 7). A transparent, crack-free, and brown wet film can be obtained after the antisolvent drop (8,9). After annealing at 150 ℃ for 15 min, a uniform and mirror like perovskite large area film is formed (10, 11, 12). Please check the attached video file for more details. The large-area film was divided into 25 pieces with dimension of 2.0 × 2.0 cm^2 to investigate the homogeneity of photovoltaic performance of PSCs; Fig. S18b and S18c). As shown in Fig. S18d, surface and cross section SEM images of large films (centre, middle, and edge) show slight deviation and the grain size is similar to that of the unit cell. Fig. S18e shows the power conversion efficiency (PCE) distribution for each divided unit cell; we achieved an average PCE of 22.27% and maximum PCE of 22.78% for the 25 subdivided PCSs (Table S3), confirming the good uniformity of large-scale incorporation with FASCl.

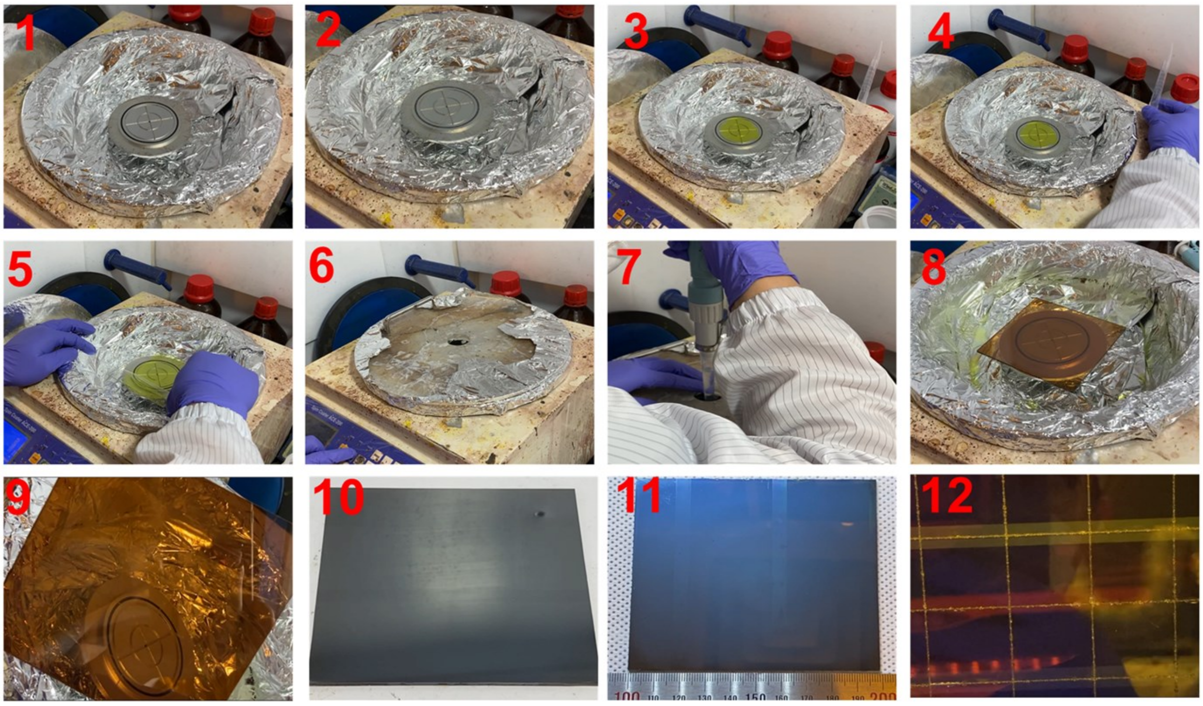

Figure S18-1. 10×10 cm^2 large area device deposition flow diagram.

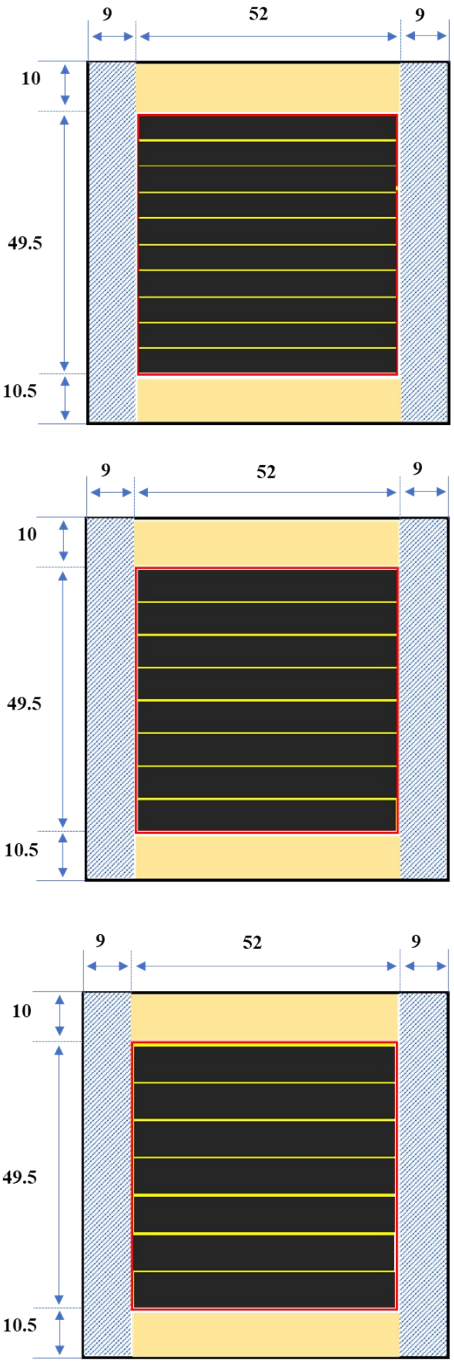

10 Sub-cell

Each sub width 5 mm

P1 (0.10 mm), P2 (0.10 mm), P3 (0.10 mm)

P12 (0.10 mm), P23 (0.10 mm)

W_a= 4.5 mm W_d= 0.5 mm

GFF= $W_a/(W_a+W_d)$= 90.0%

Total area= 25.74 cm^2

Active area= 23.17 cm^2

8 Sub-cell

Each sub width 6.25 mm

P1 (0.10 mm), P2 (0.10 mm),P3 (0.10 mm)

P12 (0.15 mm), P23 (0.15 mm)

W_a= 5.65 mm W_d= 0.6 mm

GFF= $W_a/(W_a+W_d)$= 90.4%

Total area= 25.74 cm^2

Active area= 23.27 cm^2

7 Sub-cell

Each sub width 7.15 mm

P1 (0.10 mm), P2 (0.10 mm), P3 (0.10 mm)

P12 (0.15 mm), P23 (0.15 mm)

W_a= 6.55 mm W_d= 0.6 mm

GFF= $W_a/(W_a+W_d)$= 91.6%

Total area= 25.74 cm^2

Active area= 23.58 cm^2

Figure S19. Module design details for the 25.74 cm^2 device with 7, 8, or 10 sub-cells.

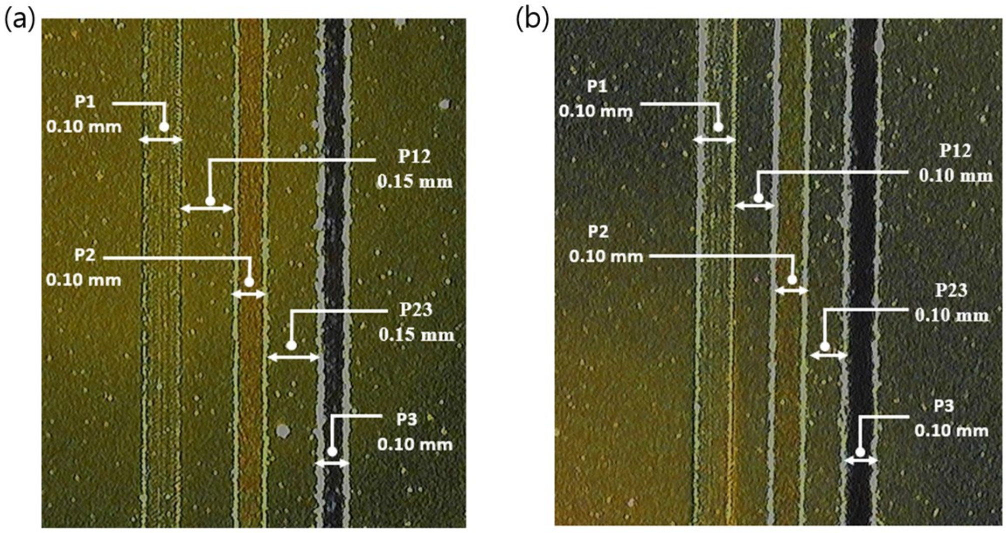

Figure S20. Optical microscopic images of the P1, P2, and P3 etched lines for module fabrication.

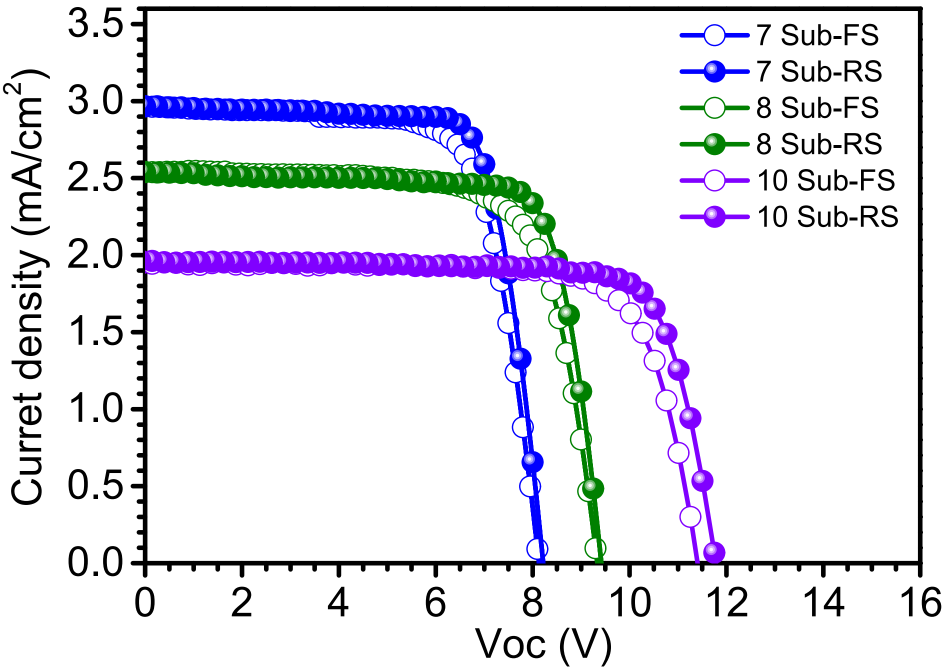

Figure S21. Current density–voltage (*J*–*V*) curves of the optimal 25.74 cm^2 perovskite solar module (PSM) prepared with different sub cells under forward (FS) and reverse (RS) scans (4 mol.%-FASCl-doped $FAPbI_3$ was used for the light-absorbing layer).

Note for figures S19–S21. In this work, we upscaled the process and developed 25.74 and 65.22 cm^2 PSMs with several sub-cell designs. Generally, when PSCs are scaled up to larger areas, the most significant PCE losses are because of the increased series resistance caused by the limited sheet conductivity of most transparent conductive oxides. The high resistivity can be partially compensated and recovered by connecting thin strips of PSCs in series connection into the PSMs. Hence, in our 25.74 cm^2 module, we tested different sub-cell effects by using 7, 8, or 10 sub-cells in a series; details of the module design are shown in in Fig. S19 and Fig. S20. Fig. S21 exhibits the *J–V* curves of the four optimal modules with different sub-cells (Table S4 lists the corresponding parameters of each module). The maximum PCE for the 7 sub-cells module (aperture area of 25.74 cm^2) was 18.71% with V_{oc} of 8.217 V, J_{SC} of 2.966 mA cm^{-2}, and FF of 0.768 under revers scan; the maximum PCE was 17.58% for the forward scan. For a designated area of 23.17 cm^2, the corresponding active area efficiency of the optimal PSM was up to 20.43% for the reverse scan and 19.19% for the forward scan with a GFF of 90.0%. The PCE was further enhanced for 8 sub-cells, with maximum PCEs of 18.76% for the reverse scan and 17.54% for the forward scan. The corresponding active area (23.27 cm^2) efficiency of the best 8 sub-cell PSM was up to 20.75% for the reverse scan and 19.41% for the forward scan with a GFF of 90.4%. However, the best performance for the 10 sub-cell device was relatively low (reverse scan: 17.94%, forward scan: 16.85%), owing to the higher series resistance causing a lower J_{SC}.

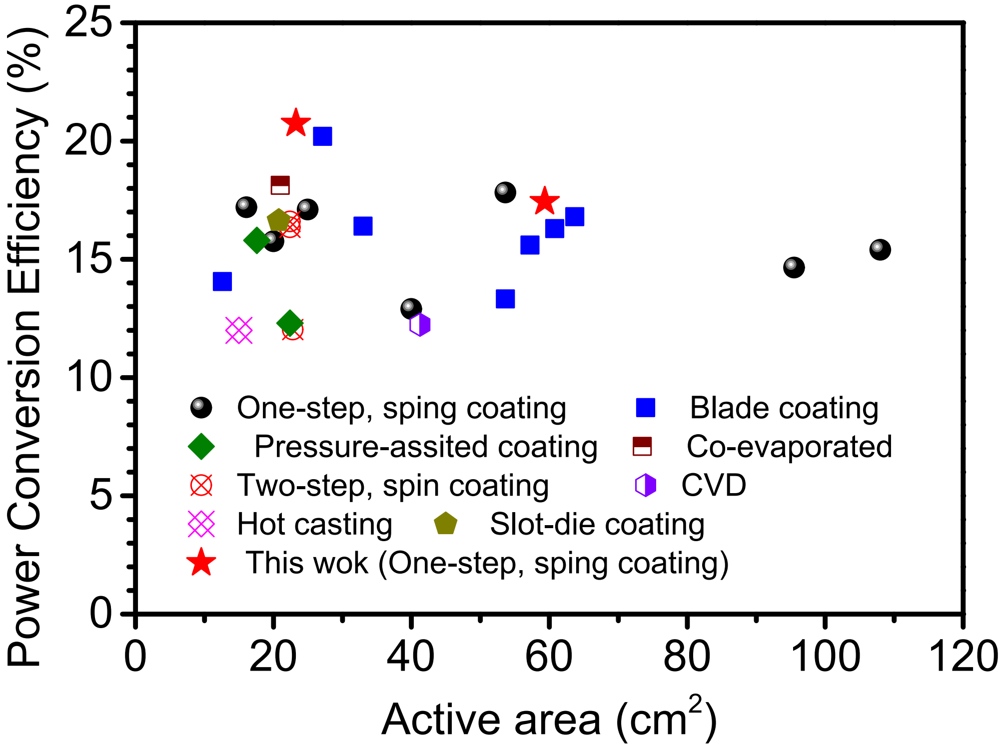

Figure S22. PCE of the PSMs as a function of the reported area from this work and other fabrication techniques. PCE was calculated based on the active area.

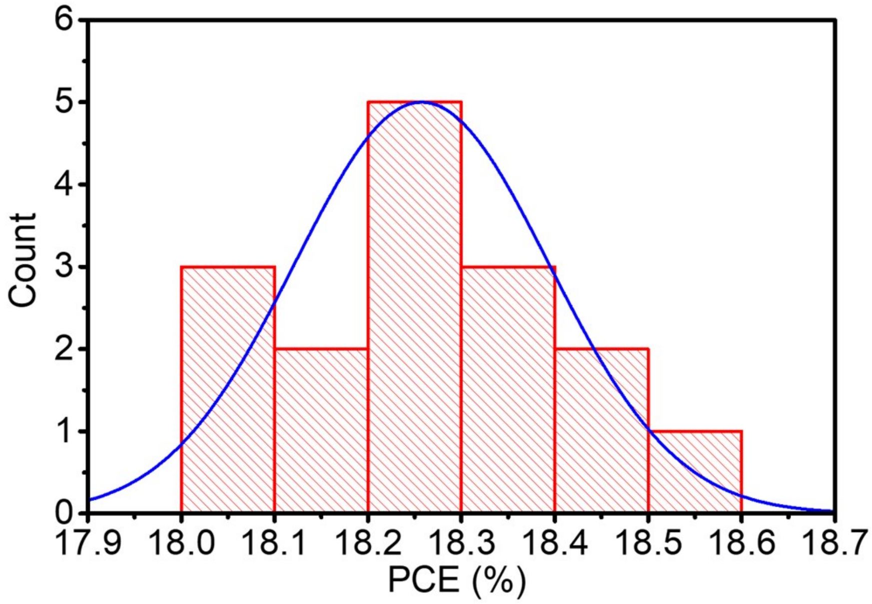

Figure S23. PCE distribution for 16 25.74 cm^2 modules based on eight sub-cells (average 18.25%).

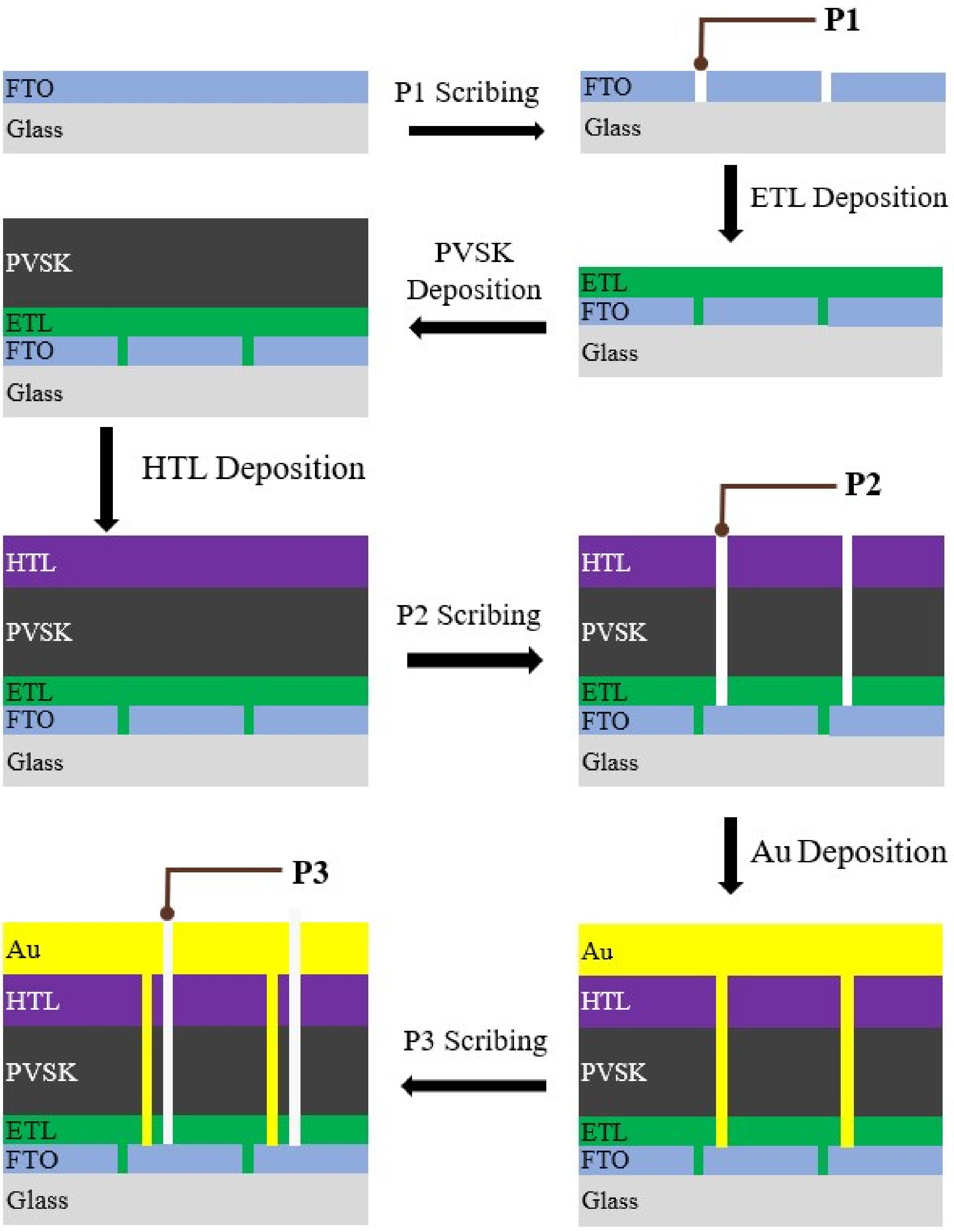

Figure S24. Flowchart for the PSM fabrication process.

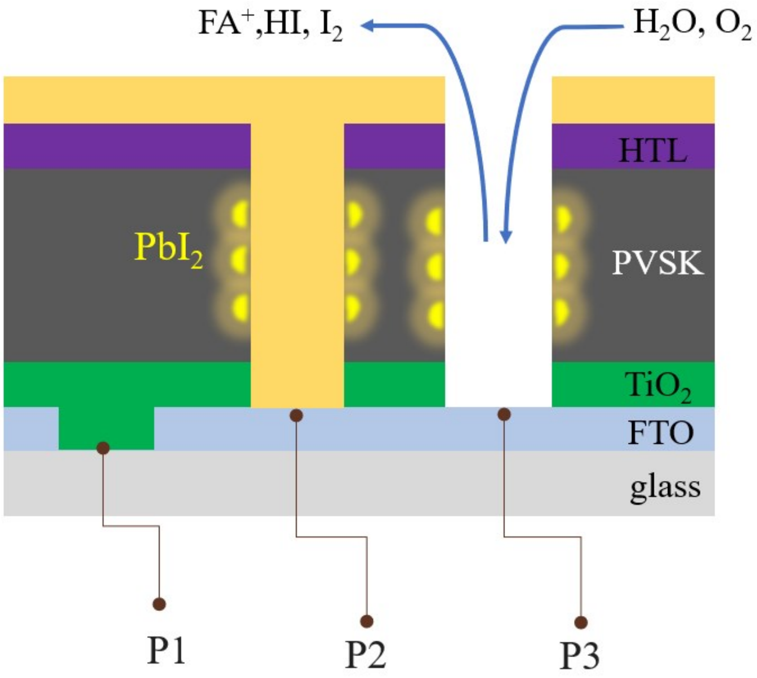

Figure S25. Potential damage mechanism during the laser scribing process.

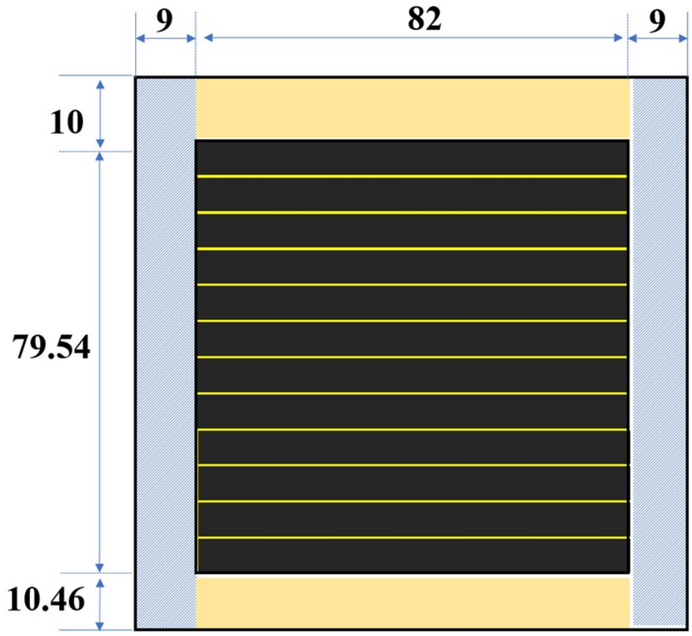

12 Sub-cell
Each sub width 6.67 mm
P1 (0.10 mm), P2 (0.10 mm), P3 (0.10 mm)
P12 (0.15 mm), P23 (0.15mm)
W_a= 6.07 mm, W_d=0.6 mm
GFF= $W_a/(W_a+W_d)$= 91.00%
Total area= 65.22 cm^2
Active area= 59.35 cm^2

Figure S26. Module design details for a 65.22 cm^2 device with 12 sub-cells.

Supplementary Tables

Table S1. Fitted parameters for the time-resolved photoluminescence (PL) decay profile of each perovskite film. TRPL fitting results obtained using the bi-exponential decay equation $I(t) = I_0 + A_1 \exp(-t/\tau_1) + A_1 \exp(-t/\tau_2)$, in which A_1 and τ_1 are the amplitude and time constant for the fast decay component, respectively, and A_2 and τ_2 are the amplitude and time constant for the slow decay component, respectively. The average PL lifetime ($\tau_{average}$) was calculated using: $\tau_{average} = (A_1\tau_1^2 + A_2\tau_2^2)/(A_1\tau_1 + A_2\tau_2)$. Compared with pristine FAPbI3, the fast decay component (τ_1) increased from 1.47 to 2.27 (control) and 2.57 ns (target), while τ_2 was significantly elongated from 182.70 (pristine) to 326.02 (control) and 779.16 ns (target). The excitation wavelength was 464 nm.

Type	A_1 (%)	τ_1 (ns)	A_2 (%)	τ_2 (ns)	$\tau_{average}$ (ns)
Pristine	294.01	1.47	263.59	182.70	181.09
Control	433.08	2.27	691.02	326.02	324.62
Target	722.05	2.57	1534.28	779.16	777.96

Table S2. V_{TFL} values obtained by fitting the dark *J–V* curves. The relationship of $\varepsilon = (C_gL)/(\varepsilon_0A)$ was used to calculate the dielectric constant of the perovskites, where C_g is the geometrical capacitance of the perovskite layer, the permittivity of free space is $\varepsilon_0 = 8.85 \times 10^{-14}$ F cm^{-1}, and A is the active area of the FTO/TiO_2/perovskite film/PCBM/Au. Abbreviations: Capacitance (C), contact area (A), thickness (d), trap-filled-limit voltage (V_{TFL}), relative dielectric constant (ε), defect density (n_t) of perovskite films based different device.

Devices	C ($\times 10^{-8}$ F)	Area (cm^2)	Thickness (nm)	V_{TFL} (V)	ε	n_{trap} ($\times 10^{16}$ cm^{-3})
$FAPbI_3$	1.69	0.225	582	0.765	50.92	1.23
FAMA	1.42	0.238	595	0.516	40.45	0.64
4 mol.%-FASCl	1.37	0.244	605	0.285	38.06	0.33

Table S3. PCE distributions of the best-performing perovskite solar cells (PSCs) in each divided device. Photovoltaic parameters of PSCs were obtained from reverse-scanned *J–V* curves. The numbers in each position represents each part of a 10 × 10 matrix (see Fig. S18b)

X Y	1	2	3	4	5
1	22.68	21.95	21.9	21.9	21.87
2	22.67	21.89	22.42	22.42	22.3
3	22.45	22.37	22.27	22.27	22.55
4	22.23	22.37	22.17	22.17	21.82
5	22.78	21.93	22.42	22.42	22.54

Table S4. Optimal photovoltaic parameters of modules with different sub-cells based on aperture area (25.74 cm^2). Abbreviations: V_{oc}, open-circuit voltage; J_{sc}, short-circuit current density; FF, fill factor; HI, hysteresis index; PCE, power conversion efficiency.

Sub-cells	J_{sc} (mA/cm^2)	V_{oc} (V)	FF	PCE (%)	HI
7-R	2.966	8.217	0.768	18.717	0.06
7-F	2.963	8.131	0.731	17.589	
8-R	2.538	9.418	0.785	18.763	0.06
8-F	2.537	9.335	0.741	17.549	
10-R	1.948	11.766	0.783	17.943	0.06
10-F	1.943	11.394	0.761	16.848	

Table S5. PCE of PSCs with different areas from other studies. Abbreviations: ®, reverse scan; No, not mentioned; FF, fill factor; HI, hysteresis index

No.	Journal (year)	Deposition methods	Active area (cm^2)	PCE (%)®	FF (%)®	HI (%)	SPO (%)
1	Joule (2020)[18]	Co-evaporated	21.00	18.13	73.4	10.6	17.2
2	Nature (2019)[19]	One-step, spin coating	24.97	17.10	72.6	9.9	No
3	Sol. RRL (2019)[20]	One-step, spin coating	53.64	17.82	69.6	1.7	No
4	Adv. Func. Mat.(2019)[21]	Two-step	22.80	12.03	61.3	No	No
5	Nat. Energy (2020)[22]	Two-step	22.40	16.60	71.0	13.9	15.9
6	Energy Environ. Sci.(2017)[23]	One-step, spin coating	20.00	15.76	65.0	1.3	No
7	Sci. Adv.(2019)[24]	Blade-coating	63.70	16.80	75.3	1.2	15.2
8	Adv. Func. Mat. (2019)[21]	Pressure-assisted coating	22.40	12.30	61.3	8.5	No
9	Acs Energy Lett. (2019)[25]	One-step, spin coating	95.50	14.65	68.0	2.1	No
10	Nat. Commun.(2018)[26]	One-step, spin coating	16.10	15.20	69.0	~0	No
11	J. Mater. Chem. A. (2018)[27]	CVD	41.25	12.24	52.8	5.4	No
12	J. Mater. Chem. A. (2020)[28]	Blade-coating	53.64	13.32	62.0	No	No
13	Adv. Energy Mater (2016) [29]	Hot casting	15.00	12.00	58.2	No	No
14	Acs Energy Lett. (2019)[30]	One-step, spin coating	108.00	13.40	65.0	No	No
15	Energy Environ. Sci.(2015)[31]	One-step, Spin coating	40.00	12.90	63.7	No	No
16	Nature (2017)[32]	Pressure-assisted coating	17.60	15.80	75.7	11.5	No
17	Nat. Energy (2018)[33]	Blade-coating	12.60	14.06	67.8	29.4	13.3
18	Nat. Energy (2018)[34]	Blade-coating	33.00	16.40	72.1	5.3	16.3
19	Nat. Energy (2018)[34]	Blade-coating	57.20	15.60	68.9	5.2	15.5
20	Nat. Energy (2021)[35]	Blade-coating	27.14	20.20	75.4	No	20.2
21	Sci. Adv. (2021)[36]	Slot-die coating	20.77	16.63	74.3	No	No
22	Nat. Sustain. (2021)[37]	blade coating	60.80	16.30	74.7	No	No
23	Adv. Energy Mater. (2021)[38]	Two-step	22.40	16.35	67.2	11.9	No
This work		**Spin coating**	**23.27**	**20.75**	**78.5**	**6.1**	**19.8**
			59.35	**17.44**	**75.3**	**10.6**	**No**

References

1. Y. Zhang, S. Seo, S. Y. Lim, Y. Kim, S.-G. Kim, D.-K. Lee, S.-H. Lee, H. Shin, H. Cheong and N.-G. Park, *ACS Energy Letters*, 2020, **5**, 360-366.
2. M. Niederberger, M. H. Bartl and G. D. Stucky, *Chemistry of Materials*, 2002, **14**, 4364-4370.
3. J. Wang, J. Polleux, J. Lim and B. Dunn, *The Journal of Physical Chemistry C*, 2007, **111**, 14925-14931.
4. H. Zhou, Q. Chen, G. Li, S. Luo, T.-b. Song, H.-S. Duan, Z. Hong, J. You, Y. Liu and Y. Yang, *Science*, 2014, **345**, 542.
5. Y. Zhou, H. Xue, Y.-H. Jia, G. Brocks, S. Tao and N. Zhao, *Advanced Functional Materials*, 2019, **29**, 1905739.
6. G. Kresse and J. Furthmüller, *Computational Materials Science*, 1996, **6**, 15-50.
7. G. Kresse and J. Furthmüller, *Physical review. B, Condensed matter*, 1996, **54**, 11169-11186.
8. J. P. Perdew, K. Burke and M. Ernzerhof, *Physical Review Letters*, 1997, **78**, 1396-1396.
9. P. E. Blöchl, *Physical Review B*, 1994, **50**, 17953-17979.
10. S. Grimme, J. Antony, S. Ehrlich and H. Krieg, *The Journal of Chemical Physics*, 2010, **132**, 154104.
11. A. A. Petrov, E. A. Goodilin, A. B. Tarasov, V. A. Lazarenko, P. V. Dorovatovskii and V. N. Khrustalev, *Acta Crystallogr E Crystallogr Commun*, 2017, **73**, 569-572.
12. J. Wang, S. Luo, Y. Lin, Y. Chen, Y. Deng, Z. Li, K. Meng, G. Chen, T. Huang, S. Xiao, H. Huang, C. Zhou, L. Ding, J. He, J. Huang and Y. Yuan, *Nature Communications*, 2020, **11**, 582.
13. J. Li, R. Munir, Y. Fan, T. Niu, Y. Liu, Y. Zhong, Z. Yang, Y. Tian, B. Liu, J. Sun, D.-M. Smilgies, S. Thoroddsen, A. Amassian, K. Zhao and S. Liu, *Joule*, 2018, **2**, 1313-1330.
14. S. Ahmad, P. Fu, S. Yu, Q. Yang, X. Liu, X. Wang, X. Wang, X. Guo and C. Li, *Joule*, 2019, **3**, 794-806.
15. Y. Zheng, T. Niu, X. Ran, J. Qiu, B. Li, Y. Xia, Y. Chen and W. Huang, *Journal of Materials Chemistry A*, 2019, **7**, 13860-13872.
16. F. Yang, M. A. Kamarudin, D. Hirotani, P. Zhang, G. Kapil, C. H. Ng, T. Ma and S. Hayase, *Solar RRL*, 2019, **3**, 1800275.
17. A. Binek, F. C. Hanusch, P. Docampo and T. Bein, *The Journal of Physical Chemistry Letters*, 2015, **6**, 1249-1253.
18. J. Li, H. Wang, X. Y. Chin, H. A. Dewi, K. Vergeer, T. W. Goh, J. W. M. Lim, J. H. Lew, K. P. Loh, C. Soci, T. C. Sum, H. J. Bolink, N. Mathews, S. Mhaisalkar and A. Bruno, *Joule*, 2020, **4**, 1035-1053.
19. E. H. Jung, N. J. Jeon, E. Y. Park, C. S. Moon, T. J. Shin, T.-Y. Yang, J. H. Noh and J. Seo, *Nature*, 2019, **567**, 511-515.
20. T. Bu, X. Liu, J. Li, W. Huang, Z. Wu, F. Huang, Y.-B. Cheng and J. Zhong, *Solar RRL*, 2020, **4**, 1900263.
21. L. Qiu, Z. Liu, L. K. Ono, Y. Jiang, D.-Y. Son, Z. Hawash, S. He and Y. Qi, *Advanced Functional Materials*, 2019, **29**, 1806779.
22. Z. Liu, L. Qiu, L. K. Ono, S. He, Z. Hu, M. Jiang, G. Tong, Z. Wu, Y. Jiang, D.-Y. Son, Y. Dang, S. Kazaoui and Y. Qi, *Nature Energy*, 2020, **5**, 596-604.
23. T. Bu, X. Liu, Y. Zhou, J. Yi, X. Huang, L. Luo, J. Xiao, Z. Ku, Y. Peng, F. Huang, Y.-B. Cheng and J. Zhong, *Energy & Environmental Science*, 2017, **10**, 2509-2515.
24. Y. Deng, C. H. Van Brackle, X. Dai, J. Zhao, B. Chen and J. Huang, *Science Advances*, 2019, **5**, eaax7537.
25. G. S. Han, J. Kim, S. Bae, S. Han, Y. J. Kim, O. Y. Gong, P. Lee, M. J. Ko and H. S. Jung, *ACS Energy Letters*, 2019, **4**, 1845-1851.
26. T. Bu, J. Li, F. Zheng, W. Chen, X. Wen, Z. Ku, Y. Peng, J. Zhong, Y.-B. Cheng and F. Huang, *Nature Communications*, 2018, **9**, 4609.

27. L. Luo, Y. Zhang, N. Chai, X. Deng, J. Zhong, F. Huang, Y. Peng, Z. Ku and Y.-B. Cheng, *Journal of Materials Chemistry A*, 2018, **6**, 21143-21148.
28. J. Zhang, T. Bu, J. Li, H. Li, Y. Mo, Z. Wu, Y. Liu, X.-L. Zhang, Y.-B. Cheng and F. Huang, *Journal of Materials Chemistry A*, 2020, **8**, 8447-8454.
29. H.-C. Liao, P. Guo, C.-P. Hsu, M. Lin, B. Wang, L. Zeng, W. Huang, C. M. M. Soe, W.-F. Su, M. J. Bedzyk, M. R. Wasielewski, A. Facchetti, R. P. H. Chang, M. G. Kanatzidis and T. J. Marks, *Advanced Energy Materials*, 2017, **7**, 1601660.
30. A. Agresti, S. Pescetelli, A. L. Palma, B. Martín-García, L. Najafi, S. Bellani, I. Moreels, M. Prato, F. Bonaccorso and A. Di Carlo, *ACS Energy Letters*, 2019, **4**, 1862-1871.
31. J. H. Heo, H. J. Han, D. Kim, T. K. Ahn and S. H. Im, *Energy & Environmental Science*, 2015, **8**, 1602-1608.
32. H. Chen, F. Ye, W. Tang, J. He, M. Yin, Y. Wang, F. Xie, E. Bi, X. Yang, M. Grätzel and L. Han, *Nature*, 2017, **550**, 92-95.
33. M. Yang, Z. Li, M. O. Reese, O. G. Reid, D. H. Kim, S. Siol, T. R. Klein, Y. Yan, J. J. Berry, M. F. A. M. van Hest and K. Zhu, *Nature Energy*, 2017, **2**, 17038.
34. Y. Deng, X. Zheng, Y. Bai, Q. Wang, J. Zhao and J. Huang, *Nature Energy*, 2018, **3**, 560-566.
35. Y. Deng, S. Xu, S. Chen, X. Xiao, J. Zhao and J. Huang, *Nature Energy*, 2021, DOI: 10.1038/s41560-021-00831-8.
36. Z. Yang, W. Zhang, S. Wu, H. Zhu, Z. Liu, Z. Liu, Z. Jiang, R. Chen, J. Zhou, Q. Lu, Z. Xiao, L. Shi, H. Chen, L. K. Ono, S. Zhang, Y. Zhang, Y. Qi, L. Han and W. Chen, *Science Advances*, 2021, **7**, eabg3749.
37. S. Chen, Y. Deng, X. Xiao, S. Xu, P. N. Rudd and J. Huang, *Nature Sustainability*, 2021, DOI: 10.1038/s41893-021-00701-x.
38. G. Tong, D.-Y. Son, L. K. Ono, Y. Liu, Y. Hu, H. Zhang, A. Jamshaid, L. Qiu, Z. Liu and Y. Qi, *Advanced Energy Materials*, 2021, **11**, 2003712.